## Quantum-informed machine learning for the prediction of chaotic dynamical systems

Maida Wang,<sup>1,\*</sup> Xiao Xue,<sup>1,\*</sup> Mingyang Gao,<sup>1</sup> and Peter V. Coveney<sup>1,2,3,†</sup>

<sup>1</sup>Centre for Computational Science, Department of Chemistry, University College London, London, UK

<sup>2</sup>Informatics Institute, University of Amsterdam, Amsterdam, The Netherlands

<sup>3</sup>Centre for Advanced Research Computing, University College London, UK

We introduce a quantum-informed machine learning (QIML) framework for the long-term dynamical behavior of high-dimensional chaotic systems. The method combines a one-time, offline-trained quantum generative model with a classical autoregressive predictor for spatiotemporal field generation. The quantum model learns a quantum prior (Q-Prior) that guides the representation of small-scale interactions and improves the modeling of fine-scale dynamics. We evaluate QIML on three representative systems: the Kuramoto-Sivashinsky equation, two-dimensional Kolmogorov flow, and a cross-section of fully developed three-dimensional turbulent channel flow used as a realistic inflow condition. Compared to the classical baseline, QIML yields up to 17.25% improvement in predictive distribution accuracy and a 29.36% improvement in the fidelity of the predicted full energy spectrum. For turbulent channel inflow, the Q-Prior is essential: without it, the model fails to evolve in time, while QIML produces stable, physically consistent forecasts that surpass leading machine learning models for PDEs, including the Fourier Neural Operator and Markov Neural Operator, whose errors diverge. Beyond accuracy, QIML also achieves a memory advantage, compressing multi-megabyte datasets into a kilobyte-scale Q-Prior that captures only the invariant measure needed to guide the classical model, thus circumventing Holevo's bound by avoiding full data reconstruction. Our findings provide a practical and scalable pathway for integrating the advantages brought by quantum devices into large-scale scientific, engineering modeling and simulation.

#### I. INTRODUCTION

Modeling high-dimensional dynamical systems remains one of the most persistent challenges in computational science. Partial differential equations (PDEs) provide the mathematical backbone for describing a wide range of nonlinear, spatiotemporal processes across scientific [1–3] and engineering domains [4]. However, high-dimensional systems are notoriously sensitive to initial conditions and the floating-point numbers used to compute them [5–8], making it highly challenging to extract stable, predictive models from data. Modern machine learning techniques often struggle in this regime: while they may fit shortterm trajectories, they fail to learn the invariant statistical properties that govern long-term system behavior. These challenges are compounded in high-dimensional settings, where data are highly nonlinear and contain complex multi-scale spatio-temporal correlations.

Machine learning has seen transformative success in domains such as large language models [9–12], computer vision [13–16], and weather forecasting [17–20], and it is increasingly being adopted in scientific disciplines under the umbrella of scientific machine learning [21, 22]. In fluid mechanics, in particular, ML has been used to model complex flow phenomena, including wall modeling [23, 24], subgrid-scale turbulence [25, 26], and direct flow field generation [27, 28]. Physics-informed neural networks [29] attempt to inject domain knowledge into the learning process, yet even these models struggle with the long-term stability and generalization issues

that high-dimensional dynamical systems demand. To address this, generative models such as Generative Adversarial Networks (GAN) [30] and operator-learning architectures like DeepONet [31] and Fourier Neural Operators (FNO) [32] have been proposed. While neural operators offer discretization invariance and strong representational power for PDE-based systems, they still suffer from error accumulation and prediction divergence over long horizons, particularly in turbulent and other chaotic regimes [33, 34]. Recent work, such as Dyslim [35], enhances stability by leveraging invariant statistical measures. However, these methods depend on estimating such measures from trajectory samples, which can be computationally intensive and inaccurate in all forms of chaotic systems, especially in high-dimensional cases. These limitations have prompted exploration into alternative computational paradigms. Quantum machine learning (QML) has emerged as a possible candidate due to its ability to natively represent and manipulate high-dimensional probability distributions in Hilbert space [36]. Quantum circuits can exploit entanglement and interference to express rich, non-local statistical dependencies using fewer parameters than their promising counterparts, which makes them well-suited for capturing invariant measures in high-dimensional dynamical systems, where long-range correlations and multimodal distributions frequently arise [37]. QML and quantum inspired machine learning have already demonstrated potential in fields such as quantum chemistry [38–40], combinatorial optimization [41–43], and generative modeling [44-47]. However, the field is constrained on two fronts: fully quantum approaches are limited by noisy intermediate-scale quantum (NISQ) hardware noise and scalability [48], while quantum-inspired algorithms, be-

<sup>\*</sup> These authors contributed equally to this work.

<sup>†</sup> p.v.coveney@ucl.ac.uk

ing classical simulations, cannot natively leverage crucial quantum effects like entanglement to efficiently represent the complex, non-local correlations found in such systems. These challenges limit the standalone utility of QML in scientific applications today. Instead, hybrid quantum-classical models provide a promising compromise, where quantum submodules work together with classical learning pipelines to improve expressivity, data efficiency, and physical fidelity. In quantum chemistry, this hybrid paradigm has proven feasible, notably through quantum mechanical/molecular mechanical (QM/MM) coupling [49–51], where classical force fields are augmented with quantum corrections. Within such frameworks, techniques like quantum-selected configuration interaction (QSCI) [52] have been employed to enhance accuracy while keeping quantum resource requirements tractable.

Quantum-enhanced machine learning (QEML) combines the representational richness of quantum models with the scalability of classical learning. By leveraging uniquely quantum properties such as superposition and entanglement, QEML can explore richer feature spaces and capture complex correlations that are challenging for purely classical models. Recent successes in quantum-enhanced drug discovery [53], where hybrid quantum-classical generative models have produced experimentally validated candidates rivaling stateof-the-art classical methods, demonstrate the practical potential of QEML even before full quantum advantage is achieved. Despite these strengths, practical barriers remain. QEML pipelines require repeated quantum-classical communication during training and rely on costly quantum data-embedding and measurement steps. which slow computation and limit accessibility across research institutions. Moreover, most current QEML applications focus on microscopic problems, such as atomic and molecular systems in quantum chemistry, with little exploration of macroscopic phenomena like nonlinear PDEs and turbulent flows, where long-term stability and statistical fidelity pose distinct challenges.

To address these limitations, we propose a Quantum-Informed Machine Learning (QIML) architecture for chaotic systems. The quantum component is a samplebased quantum generator grounded on the quantum circuit Born machine [54, 55], trained once offline on quantum hardware to learn invariant statistical properties directly from observational data. The resulting compact quantum prior (Q-Prior) can be deployed broadly and efficiently without ongoing quantum-classical iteration, eliminating the need for repeated access to quantum hardware during training. This design is specifically tailored to learning the dynamics of nonlinear PDEs. These properties capture complex, high-dimensional distributions compactly by leveraging entangled quantum states. Unlike standard deep-learning surrogates, such as fully connected or convolutional networks that require large parameter counts to represent such structures, the quantum generators operate in exponentially large Hilbert

spaces, enabling expressive modeling with as few as 10 to 15 qubits for the systems in this paper. Crucially, this framework circumvents the data-loading bottleneck common to many QML algorithms. The generator does not need to encode raw data onto quantum states; instead, it learns a compressed, generative model of the data's underlying statistical properties. The model is trained with a sample-based Maximum Mean Discrepancy (MMD) loss [56], enabling it to learn the quantum representation without knowing the data distribution. After the training of the quantum generator, the resulting Q-prior is then integrated into an autoregressive, unitary-enhanced Koopman-based machine learning framework [57]. This architecture is powerful for learning dynamical systems as it can linearize nonlinear dynamics in a lifted observable space, making it effective for capturing coherent structures [58, 59]. However, for high-dimensional chaotic systems, its ability to maintain predictive stability remains a significant challenge, often failing to preserve the systems' physical invariant measures over extended rollouts (i.e. recursive 1-in-1out predictions where each forecasted state is fed back as input for the next step). This is particularly true when modeling data for which no closed-form governing equation is known—as is the case for a two-dimensional cross-section extracted from a three-dimensional turbulent domain. We address this limitation by embedding the Q-prior as a differentiable constraint directly within the loss function. This composite loss, which penalizes divergence from the Q-prior, imposes a powerful statistical regularization on the evolution of the Koopman operator, guiding it to learn a physically consistent and stable longterm dynamic. We evaluate our QIML framework against its classical counterpart without Q-informed guidance, as well as two leading machine learning models: the FNO for general PDE-based systems and the Markov Neural Operator (MNO) specifically designed for chaotic dynamics. Our QIML framework outperforms all baseline models, which fail to sustain stable rollouts over time, leading to divergence and loss of physical consistency.

The remainder of this paper is structured as follows. In Sec. II, we detail the architecture of our QIML framework, including the Koopman operator formulation and the integration of the quantum prior. In Sec. III, we present the evaluation of our framework on three canonical chaotic systems. A direct comparative analysis of QIML against state-of-the-art classical machine learning baselines is provided in Sec. IV. We then discuss the profound memory efficiency of the Q-Prior in Sec. V. Finally, we conclude in Sec. VIII and offer a discussion on the limitations and future outlook of this work in Sec. VII.

## II. QUANTUM-INFORMED MACHINE LEARNING FRAMEWORK

In this section, we present the QIML architecture that leverages a quantum-classical hybrid approach for ma-

## The Structure of the Quantum-Informed Machine Learning

## a. Data generation

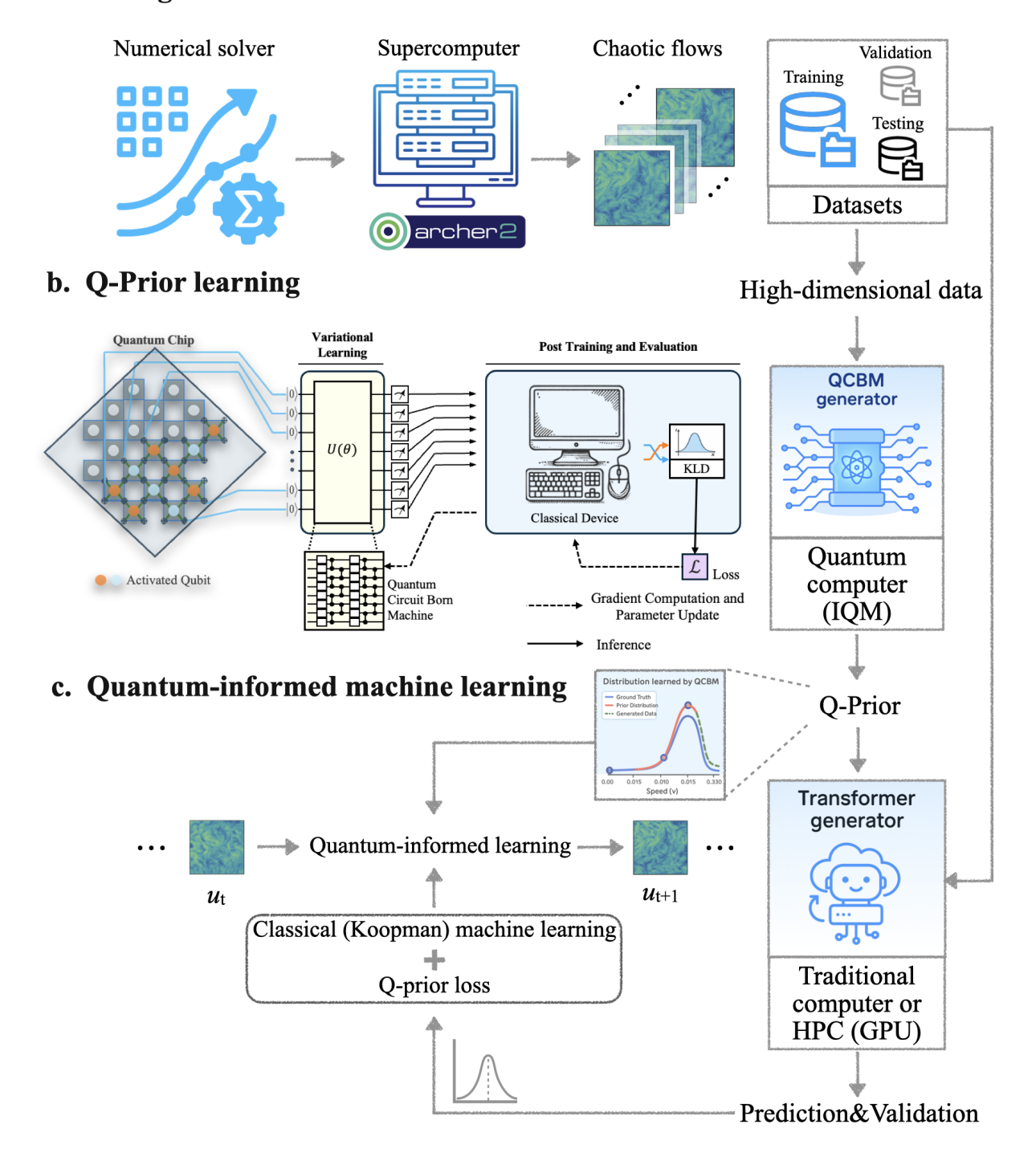


FIG. 1. Architecture of the QIML framework. a. High-dimensional dynamical flow fields are generated using high-resolution numerical solvers and used to construct training, validation and test datasets. b. A quantum circuit is trained on superconducting hardware to learn invariant statistical properties from the data (Q-Prior). c. The learned Q-Prior is integrated into a classical transformer machine learning, guiding it toward physically consistent predictions and improved long-term stability.

chine learning-based modeling of high-dimensional dynamical systems. Our QIML scheme is illustrated in Fig. 1. The workflow commences with the data generation stage (Fig. 1a), where we employ a numerical solver on a classical computer to simulate complex highdimensional flows, producing the necessary training, validation, and testing datasets. Subsequently, in the quantum machine learning phase (Fig. 1b), a quantum generator is implemented on a quantum computer to learn the underlying physical invariant distribution, referred to as the Q-Prior. Finally, this Q-Prior is used to inform and regularize the classical machine learning model during training (Fig. 1c), guiding it toward long-term statistical consistency with the target dynamical system. We begin by introducing the machine learning component, which is based on a Koopman operator formulation. The Koopman operator offers a linear representation of nonlinear dynamical systems by acting on observables instead of directly on the state variables. In this framework, the evolution of the system is captured not in the original state space, but in a lifted function space where the dynamics become linear. Consider a discrete-time dynamical system:

$$x_{t+1} = f(x_t), \tag{1}$$

where  $x_t \in \mathbb{R}^n$  with n denotes the dimension of the state space at time t, and f is a generally nonlinear transition function. To enable auto-regressive prediction and long-term rollouts, we aim to find a mapping from the high-dimensional space to a latent space where a linear operator governs the time evolution. The measure-preserving property in the latent space is particularly important for capturing the statistical properties and invariant measure  $\mu$  of high-dimensional dynamical systems. The Koopman operator K acts on observables  $g: \mathbb{R}^n \to \mathbb{C}$  such that:

$$(Kg)(x) = g(f(x)). (2)$$

While K is linear, our implementations seek finitedimensional approximations by learning a set of observables whose evolution under K is closed and linear. Next, we approximate the Koopman operator using a neural network; we define an encoder  $\phi: \mathbb{R}^n \to \mathbb{R}^l$ , with l denotes the latent dimension, that maps the system state into a latent (feature) space, and a decoder  $\psi: \mathbb{R}^l \to$  $\mathbb{R}^n$  that reconstructs the original state. Unlike generic autoencoders primarily focused on data reconstruction, our Koopman operator neural network is specifically designed to learn a linear, norm-preserving evolution in the latent space, which is crucial for maintaining the longterm stability and physical fidelity of high-dimensional dynamical systems. Our detailed autoencoder-decoder architecture description can be found in Appendix G for 1D and 2D cases. The dynamics in the latent space are modeled by a linear operator  $K \in \mathbb{R}^{l \times l}$ , such that:

$$z_t = \phi(x_t), \quad z_{t+1} = Kz_t, \quad \hat{x}_t = \psi(z_t),$$
 (3)

where  $z_t$  is the encoded latent state and  $\hat{x}_t$  is the reconstructed state. To preserve the long-term statistical behavior of the system and approximate the spectral properties of a measure-preserving dynamical system, we constrain the operator K to be unitary, i.e.,  $K^{\top}K = I$  [57, 60, 61]. This ensures that the Koopman dynamics in the latent space are norm-preserving and stable under long-term rollouts. In this work, unitarity is imposed by adding a regularization term to the loss function of the form  $\mathcal{L}_{\text{unitary}} = ||K^{\top}K - I||^2$ . The Koopman operator K evolves the system in a latent Hilbert space of encoded observables, enabling a linear and spectrally coherent representation of the dynamics. However, the preservation of long-term statistical properties in this latent space does not automatically guarantee consistency with the statistical structure of the original physical space.

To address this, we integrate a sample-based quantum generator, which approximates the invariant distribution Q-Prior  $p_{\theta}(x)$  of the system. This quantum-learned prior is used as a statistical regularizer and physically informed guidance during the classical machine learning training, guiding the model to produce predictions that are not only temporally coherent but also statistically consistent with the system's long-term behavior (See Method C). This integration is achieved by incorporating the Q-Prior into a composite loss function that combines reconstruction fidelity with statistical alignment metrics, which is shown below.

While the Koopman operator is introduced using a generic state variable, in this work, we focus on predicting physical states u. We use the Koopman operator to predict the next time frame of the physical states  $\hat{u}_{t+1}$ . The training of our model is guided by a composite loss function. We define its components below.

First, to ensure predictive accuracy, we use a standard reconstruction loss  $\mathcal{L}_{\text{recon}}$  which measures the mean squared error between the predicted state  $\hat{u}_{t+1}$  and the ground truth  $u_{t+1}$ :

$$\mathcal{L}_{\text{recon}} = \|\hat{u}_{t+1} - u_{t+1}\|^2$$
. (4)

Second, we include the unitary regularization term  $\mathcal{L}_{unitary}$  as previously discussed:

$$\mathcal{L}_{\text{unitary}} = \left\| K^{\top} K - I \right\|_{F}^{2}, \tag{5}$$

where I is the identity matrix and  $\|\cdot\|_F$  denotes the Frobenius norm. Finally, we incorporate the Q-prior,  $p_{\theta}(x)$ , as a statistical constraint. This is achieved through two complementary metrics. The Kullback-Leibler (KL) divergence  $\mathcal{L}_{\mathrm{KL}}$  captures low-order, information-theoretic discrepancies between the empirical distribution of predicted states  $\hat{q}(x)$ , and the Q-Prior:

$$\mathcal{L}_{KL} = D_{KL} \left( \hat{q}(x) \parallel p_{\theta}(x) \right). \tag{6}$$

To align higher-order statistical moments, we also include

a MMD term  $\mathcal{L}_{\text{MMD}}$ :

$$\mathcal{L}_{\text{MMD}} = \left\| \mathbb{E}_{x \sim \hat{q}(x)} [\phi(x)] - \mathbb{E}_{x \sim p_{\theta}(x)} [\phi(x)] \right\|_{\mathcal{H}}^{2}. \tag{7}$$

These individual components are combined into a single training objective, where the Q-Prior terms are weighted by empirically selected hyperparameters  $\lambda_{\rm KL}$  and  $\lambda_{\rm MMD}$ :

$$\mathcal{L}_{\rm total} = \mathcal{L}_{\rm recon} + \mathcal{L}_{\rm unitary} + \lambda_{\rm KL} \mathcal{L}_{\rm KL} + \lambda_{\rm MMD} \mathcal{L}_{\rm MMD}. \tag{8}$$

The full QIML framework is demonstrated in Algorithm 1. All models are implemented in PyTorch with fully differentiable integration of Q-Priors. Architectural details for predicting 1D and 2D systems are provided in Appendix G.

# **Algorithm 1** Training of the Quantum-Informed Machine Learning Model

Require: Dataset  $\{u_t, u_{t+1}\}$ , Q-Prior distribution  $p_{\theta}(x)$ 1: Initialise machine learning model parameters  $\phi$ 2: Set loss weights  $\lambda_{\text{KL}}, \lambda_{\text{MMD}}$ 3: for each training epoch do

4: **for** each mini-batch  $(u_t, u_{t+1})$  **do** 

5: Predict next-step field:  $\hat{u}_{t+1} \leftarrow f_{\phi}(u_t, \dots)$ 

6: Compute empirical distribution  $\hat{q}(x)$  from  $\hat{u}_{t+1}$ 

7: Compute reconstruction loss:

$$\mathcal{L}_{\text{recon}} \leftarrow \left\| \hat{u}_{t+1} - u_{t+1} \right\|^2$$

8: Compute unitary regularization loss:

$$\mathcal{L}_{\text{unitary}} \leftarrow \|K^{\top}K - I\|_F^2$$

9: Compute KL divergence:

$$\mathcal{L}_{\mathrm{KL}} \leftarrow D_{\mathrm{KL}}(\hat{q}(x) \parallel p_{\theta}(x))$$

10: Compute MMD loss:

$$\mathcal{L}_{\text{MMD}} \leftarrow \left\| \mathbb{E}_{x \sim \hat{q}(x)}[\phi(x)] - \mathbb{E}_{x \sim p_{\theta}(x)}[\phi(x)] \right\|_{\mathcal{H}}^{2}$$

11: Compute total loss:

$$\mathcal{L}_{\rm total} = \mathcal{L}_{\rm recon} + \mathcal{L}_{\rm unitary} + \lambda_{\rm KL} \mathcal{L}_{\rm KL} + \lambda_{\rm MMD} \mathcal{L}_{\rm MMD}$$

12: Backpropagate and update  $\phi$  via Adam optimizer

13: end for

14: end for

15: **return** Trained model  $f_{\phi}$ 

## A. Invariant measure for high-dimensional dynamical systems

The concept of an invariant measure originates from the field of ergodic theory and has become a fundamental tool in the study of dynamical systems. First formalized in the context of measure-preserving transformations by Birkhoff and von Neumann in the early 20th century, invariant measures capture the long-term statistical behavior of systems evolving under deterministic rules [62, 63]. An invariant measure describes how a dynamical system spends its time in different regions of its state space over the long term. For a system evolving under a map T, the invariant measure  $\mu(x)$  satisfies:

$$\mu(T^{-1}(A)) = \mu(A),$$
 (9)

which means that the total probability of the system being in a region A remains the same after one step of evolution. This property reflects a kind of statistical balance: although individual trajectories may change, the overall distribution stays stable. In our work, we aim to capture this long-term behavior by ensuring that the model's predictions remain consistent with a reference distribution, which we learn using a quantum generator.

In turbulent flows, such invariant measures typically manifest as conserved distributions, such as velocity probability, turbulent kinetic energy, or energy spectra that encode physical long-term steady states. Capturing these invariant features is essential for ensuring robustness in extrapolative prediction regimes, where a classical machine learning method often suffers from gradient explosion, mode collapse, or long-term error accumulation [64].

## B. The quantum generator to learn the Q-Prior

We develop a quantum-informed learning component in which a quantum generator is used to directly learn invariant statistical properties from high-dimensional physical observations. The generator defines a parameterized quantum state  $|\psi_{\theta}\rangle$  on an *n*-qubit register, which serves as a generative model over a discretised spatial domain. It does not encode a specific state (e.g., a velocity field) into the circuit. Instead, by observing many snapshots of the system, it learns to reproduce its underlying invariant probability distribution. Specifically, each computational basis state  $x \in \{0,1\}^n$  here is mapped bijectively to a spatial coordinate in the simulation grid. The corresponding amplitude  $\langle x|\psi_{\theta}\rangle$  is optimized so that its squared magnitude approximates the normalized velocity magnitude at that point. Although the circuit does not encode classical inputs directly via amplitude encoding, it constructs a quantum state whose Born distribution approximates the invariant measure Q-Prior of the system. The resulting Born distribution is given by:

$$p_{\theta}(x) = \left| \langle x | U(\theta) | 0 \rangle^{\otimes n} \right|^2, \tag{10}$$

where  $U(\theta)$  is a parameterized unitary circuit composed of L layers, each consisting of single-qubit rotations and entangling operations. Each computational basis state represents a discrete spatial point, and the quantum amplitudes are trained to reflect the empirical distribution of local velocity magnitudes. This provides a compact, data-driven mapping from physical observables into the

Hilbert space. The exponential size of this space, combined with the use of entangling gates, provides a natural mechanism to encode the complex, non-local correlations inherent in chaotic systems. This feature provides a quantum advantage rooted in the ability of quantum systems to represent high-dimensional classical data with exponential efficiency [65]. This enables it to learn the required statistical properties using exponentially fewer parameters than would be required by a classical model [66]. Furthermore, by leveraging the vast Hilbert space and entanglement, the quantum circuit can capture the complex, non-local correlations inherent in such systems efficiently [67]. Further details can be found in section VI and Appendix A.

As shown in Algorithm 2, the quantum circuit is trained as a quantum generative model. Each computational basis state  $x \in \{0,1\}^n$  is mapped uniquely to a spatial location  $\mathbf{r}_x$  in the discretised velocity field, and its target value is the corresponding velocity magnitude  $u(\mathbf{r}_x)$ . Because the underlying probability distribution over spatial locations is unknown, we adopt a sample–based training strategy that minimises the MMD loss:

$$\mathcal{L}_{\text{MMD}}(\theta) = \left\| \frac{1}{N} \sum_{i=1}^{N} \phi(x_i) - \frac{1}{M} \sum_{j=1}^{M} \phi(\tilde{x}_j) \right\|_{\mathcal{H}}^{2}, \quad (11)$$

Here,  $\{x_i\}_{i=1}^N$  denotes the batch of empirical samples drawn from the reference velocity field, while  $\{\tilde{x}_j\}_{j=1}^M \sim p_{\theta}(x)$  are samples generated by the quantum circuits. Because the MMD objective is expressed solely through kernel evaluations on finite sample sets, optimization of the generator requires no closed-form expression for the target probability density. This sample-based objective is particularly advantageous for high-dimensional chaotic flows, where the invariant measure is available only as a time-ordered set of simulation snapshots rather than an explicit probability density. By aligning the quantum generator's samples with these numerical trajectories, the model infers the underlying measure without ever needing a closed-form expression.

The trained quantum distribution  $p_{\theta}(x)$  thus can serve as a data-driven prior capturing the invariant measure of the underlying physical process. Unlike classical regularizers based on fixed heuristics, the quantum generator constructs this Q-Prior through optimization on empirical data.

All quantum circuits are implemented using hardware-efficient structures, which are detailed in Appendix B. Training is carried out on noiseless simulators and on superconducting quantum hardware, with circuit transpilation, error mitigation, and device-specific calibration performed using the Qiskit runtime. Further details and the optimization methods are provided in Appendices A and B.

**Algorithm 2** Training of the quantum generator for invariant measure

**Require:** Velocity snapshots  $\{u_t\}$ ; circuit depth L; qubits n**Ensure:** optimized parameters  $\theta^*$  such that  $p_{\theta^*}(x)$  matches the empirical distribution Initialise  $\theta \sim \mathcal{U}[-\pi, \pi]$ for each training epoch do 3: Build unitary  $U(\theta)$  (depth L, n qubits) Generate M samples  $\{\tilde{x}_j\}_{j=1}^M \sim p_{\theta}(x)$ 4: Extract N target samples  $\{x_i\}_{i=1}^N$  from  $\{u_t\}$ 5: Compute  $\mathcal{L}_{\text{MMD}}(\{x_i\}, \{\tilde{x}_j\})$ 6: 7:  $\theta \leftarrow \theta - \eta \nabla_{\theta} \mathcal{L}_{\text{MMD}}$ 8: end for 9: return  $\theta^*$ 

### C. Quantum hardware implementation

The sample-based quantum generator model was trained using both emulators on classical computers and real superconducting quantum processors. A classical emulator here is a program running on a conventional computer that simulates the mathematical operations of an ideal, noise-free quantum device. In this work, these emulations were supported by the PennyLane and Qiskit software packages. The practical constraints of current NISQ-era hardware, which require cryogenic operating temperatures and are subject to frequent maintenance and recalibration, make continuous, large-scale training across numerous datasets challenging. For this reason, we adopted a strategic approach here. The first two systems (Kuramoto-Sivashinsky and Kolmogorov flow) were studied on the classical emulator to establish the Q-Prior's efficacy in an ideal, noise-free setting. We then reserved the use of the real quantum hardware for the most complex and challenging dataset, which is the turbulent channel flow, precisely because this is the case where leading classical methods fail, providing the most stringent test for the QIML framework's practical utility and robustness under realistic noise conditions. To ensure effective execution on near-term quantum hardware and to manage the impact of noise on the quality of Q-Priors, this study constrains the total number of trainable parameters and adopts conservative circuit configurations. Specifically, the number of qubits is 10–15 on the emulator and 10 on the hardware, with circuit depths ranging from 3 to 8 layers, resulting in fewer than 300 trainable parameters in total (see Appendix B table IV). Hardware experiments were mainly conducted on IQM's 20-qubit superconducting chip (Garnet) [68, 69], using qubits 1–10 as the active subset, supported by Qiskit and IQM-Qiskit. Further discussion on hardware implementation and sensitivity is provided in Appendix B. To ensure scalability, the quantum emulation and hardware backend were integrated into a GPU-accelerated classical training loop on NVIDIA A100 nodes provided by the BEAST GPU cluster (Leibniz Supercomputing Centre). Gradient evaluations, loss computations, and optimizer updates were performed classically and synchronised with the quantum

hardware at each iteration. This setup constitutes an applied demonstration of embedding quantum devices into scientific machine learning pipelines.

The employed quantum circuit architecture consisted of alternating layers of parameterized  $R_x$  rotations and hardware-native entangling gates. Importantly, the same circuit structure was used across all experiments without dataset-specific tailoring, ensuring general applicability. Although performance could potentially be improved through customised ansatz design, our results demonstrate that the proposed quantum-informed framework is compatible with any hardware-efficient quantum circuit. This adaptability enables the integration of diverse circuit architectures without modifying the overall training pipeline, suggesting broad utility across problem domains and quantum backends.

The Q-prior is generated via a one-time, offline training process. This training consists of a total of 50 epochs. Following the completion of this training, the quantum circuit is not utilized during the main classical model's training loop. For each of the 50 training epochs, the circuit was sampled with 20,000 shots to ensure a highfidelity statistical distribution. Readout errors were mitigated using IQM's native transpiler and the M3 measurement mitigation toolkit [70]. While we used this number of shots to ensure maximum stability and demonstrate the framework's potential, this is not a strict requirement for its effectiveness. In separate tests, we reduced the measurement count to 8,000 shots and found the impact on the final model's performance was less than 5%, indicating that the Q-Prior remains effective. Nevertheless, to present the best possible outcomes in this work, all results and figures are based on data obtained from 20,000 shots per iteration. optimization was performed using L-BFGS [71], Adam [72], and COBYLA [73], selected based on convergence stability and noise robustness. To prevent mode collapse, such as excessive sampling concentration on the  $|0\rangle$  state, runtime monitoring and redundancy checks were incorporated into the training loop. Despite operating with only 10 to 15 qubits, the Q-Prior successfully captured the structure of invariant distributions over a 1000- to 60,000-dimensional Hilbert space, demonstrating the effectiveness of quantum priors in modeling high-dimensional systems. Further discussions of the error mitigations, experiment results, and ablations are provided in Appendices B and G.

## III. RESULTS

## A. Numerical set up

The selected test cases span increasing levels of physical and dynamical complexity. We begin with the Kuramoto–Sivashinsky (KS) equation, a PDE exhibiting spatiotemporal chaos. The solution is discretised into 512 spatial grid points, resulting in a 512-dimensional state vector at each time step. Next, we consider two-

dimensional Kolmogorov flow on a  $64 \times 64$  spatial grid (dimension = 4096), governed by the 2D incompressible Navier-Stokes equations in a periodic domain, where the quantum generator is trained in emulation to extract turbulent invariant measures. Finally, we examine cross-sections of a three-dimensional turbulent channel flow (TCF), simulated using the lattice Boltzmann method (LBM), which is numerically equivalent to solving the Navier-Stokes equations [74]. For the training process, the raw cross-sections are down-sampled and discretised onto a  $64 \times 64$  spatial grid, resulting in a 4096dimensional state vector. The Q-Prior for TCF is trained on superconducting quantum processors. While the full flow field is simulated numerically, the extracted twodimensional cross-sectional datasets used in our analysis do not satisfy any closed-form governing equation. This distinction highlights a further step in complexity: moving from lower-dimensional systems with explicit dvnamics to high-dimensional observational data without accessible evolution laws, thereby testing the capacity of QIML to generalize across different scenarios. Throughout this study, 'ground truth' or 'raw data' refers to the high-resolution simulation data generated by established numerical solvers. While this raw simulation data has a large memory footprint, the quantum-informed priors offer parameter efficiency and memory advantage. They capture the flow's essential statistical features using fewer than 300 trainable parameters, occupying only a few megabytes of storage, which corresponds to a data storage reduction of over two orders of magnitude compared to the raw data. This approach enables a substantial reduction in data storage requirements compared to using the raw simulation data (see section Method E and Appendix B-C). The classical components of the models were trained on a single NVIDIA A100 80GB GPU using default settings with 32-bit floating-point precision (for details, see Appendix D).

## B. Kuramoto-Sivashinsky equation

We first apply our QIML framework to learn the solution of the Kuramoto-Sivashinsky equation, which is given by:

$$\frac{\partial u}{\partial t} + u \frac{\partial u}{\partial x} + \nu \frac{\partial^2 u}{\partial x^2} + \mu \frac{\partial^4 u}{\partial x^4} = 0 \tag{12}$$

where u(x,t) denotes a scalar field representing the state of the system, with  $u:[0,L]\times[0,\infty)\to\mathbb{R},\,x\in[0,L]$  representing the spatial domain and  $t\in[0,\infty)$  the time;  $\nu$  and  $\mu$  are constants which are set to 1 for this study. The spatial domain is discretised using N=512 equidistant grid points. Raw data are generated as described in Appendix D. The dataset consists of 1200 trajectories, where each trajectory is made up of 2,000 time frames. The spatial domain for each frame is discretised using 512 grid points. We partition the trajectories chronologically into 80% training, 10% validation, and 10% test sets.

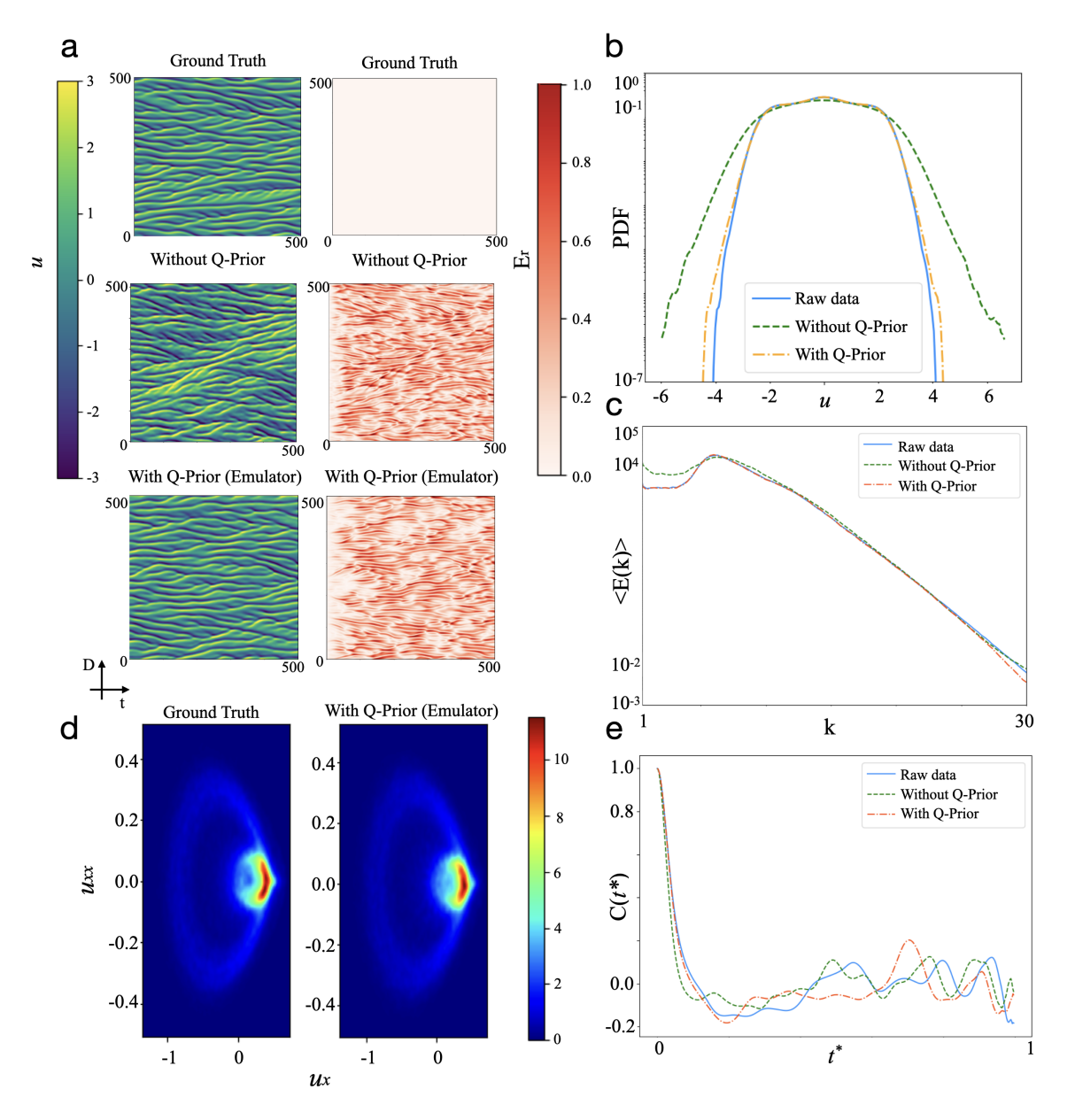


FIG. 2. Evaluation of the QIML framework on the KS system. a. This panel displays time-averaged mean velocity fields (left column) and corresponding relative error  $E_r$  maps (right column) across the ground truth, the classical ML without Q-Prior, and the quantum-informed ML model with Q-Prior (from top to bottom). b. This panel presents the probability distribution of u. c. This panel shows the energy spectrum  $\langle E(k) \rangle$  as a function of spatial wavenumber k, characterizing kinetic energy distribution across spectral modes. d. This panel visualizes the invariant density when dynamics are projected into the  $(u_x, u_{xx})$  space, revealing the geometric support of the underlying invariant measure. e. This panel plots the temporal autocorrelation, denoted by  $C(t^*)$ , computed from the time series of the field u averaged over all spatial points. The correlation is shown as a function of the dimensionless time lag  $t^* = t/t_{end}$ .

For this system, both the classical Koopman machine learning (without Q-Prior) and the main QIML model (with Q-Prior) are trained for 500 epochs. The Q-Prior for the QIML configuration is generated by a sample-based quantum generator using 10 qubits ( $2^{10}=1\,024$  basis states) and 120 trainable parameters. Full architectural and training details for both configurations are provided in Appendix G.

Fig. 2 presents the QIML evaluation results on the Kuramoto–Sivashinsky system, comparing two configurations against the numerical simulation: a classical machine learning model trained without Q-Priors (without Q-Prior), and a quantum-informed machine learning model incorporating a prior trained in simulation (with Q-Prior). Both machine learning models perform inference in an auto-regressive manner: starting from an ini-

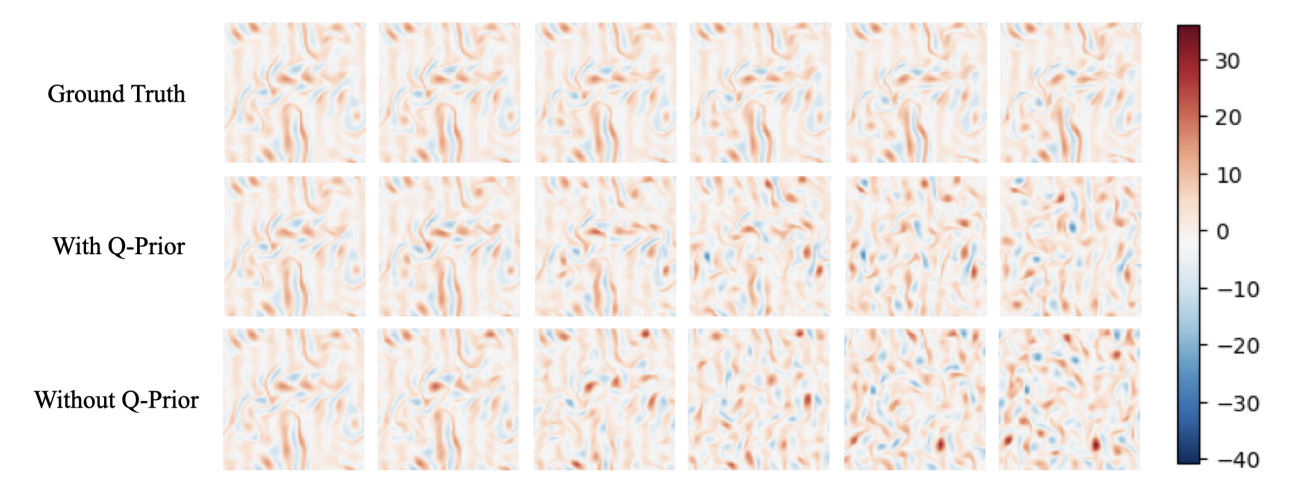


FIG. 3. The streamwise velocity rollout of ground truth (top), the QIML with Q-Prior (middle), and the classical model without Q-Prior (bottom) given the same initial state at  $\hat{t} = 0.0, 0.2, 0.4, 0.6, 0.8, 1.0$  (from left to right).

tial condition at time step  $t_0 = 0$ , the model predicts the next frame at each subsequent step and recursively continues this process up to  $t_{\rm end} = 500$  time steps to ensure long-term statistics. Panel (a) shows the u evolution alone the time: with 512 initial states and 500 prediction timesteps, and the corresponding relative error  $E_r$  evolution. The error metric definition is presented in Appendix I. From top to bottom, each row corresponds to the ground truth, the ML model without Q-Prior configuration, and the QIML model with Q-Prior configuration. These sub-panels are computed over the test dataset to visualize long-term statistical characteristics of the predictions. In the "without Q-Prior" configuration, the model reproduces the general structure of the ground truth. However, over time, the predicted stripe patterns drift upward, revealing noticeable discrepancies in the associated error map. This indicates that the model accumulates errors during long-term prediction, likely due to the absence of prior information to guide the dynamics. In contrast, the "with Q-Prior" model demonstrates much closer alignment with the ground truth. The predicted fields preserve fine-scale features and capture the parallel stripe structures effectively. Additionally, the corresponding error maps exhibit substantially lower and more spatially diffuse errors. These results suggest that incorporating the Q-Prior enhances the model's stability and accuracy in long-term forecasting. Panel (b) presents the probability density function (PDF) of u for each configuration. The distribution is obtained via the entire spatiotemporal test domain (512 states in space and 500 prediction steps in time), allowing for a comparison of global statistical fidelity. The raw test data (solid blue line) serves as the ground truth. The model without Q-Prior (green dashed line) deviates from the raw data, particularly in the tails of the distribution, where it tends to overestimate the probability. In contrast, the model with Q-Prior (orange dash-dotted line) closely matches the ground truth across the full velocity range, especially

in the tails. This improved statistical fidelity is confirmed by a quantitative analysis of the overall prediction error; the inclusion of the Q-Prior results in a 17.25% reduction in the Mean Squared Error (MSE) of the predicted fields with respect to the ground truth over the first 100 steps. This effect becomes even more pronounced in the distribution tails (events where |u| > 4), where the error is suppressed by nearly two orders of magnitude. Moreover, an analysis of the spectrum demonstrates superior performance across all energy scales, achieving a 29.36% reduction in MSE for this metric. This demonstrates that incorporating the Q-Prior generated allows the machine learning model to more accurately reproduce the statistical characteristics of the system, including rare events. Panel (c) shows the energy spectrum  $\langle E(k) \rangle$  as a function of the wave number k, comparing the raw data, the machine learning model with and without Q-Prior. The energy spectrum of the raw data follows a smooth decay with increasing k, reflecting the distribution of energy across spatial frequencies. The model without Q-Prior overestimates the energy in the large-scale, deviating from the ground truth. However, the model with Q-Prior closely aligns with the raw data across all wave numbers, able to capture both large-scale and small-scale (high-k) behavior of the system. To further visualize the invariant structures underlying the KS system, we project both the ground truth and the Q-Prior configuration into the  $(u_x, u_{xx})$  phase space, as shown in Panel (d). The resulting density plots depict the support of the system's invariant measure, providing insight into its long-term statistical behavior. Over an extended prediction, the model with Q-Prior closely aligns with the ground truth in phase space, accurately capturing the geometry and concentration of the invariant set. This qualitative agreement highlights the Q-Prior model's ability to preserve the system's underlying statistical structures over time. Panel (e) illustrates the temporal autocorrelation  $C(t^*)$ of the velocity field, averaged over all spatial points, as a

function of the dimensionless time lag  $t^* = t/t_{end}$ . Autocorrelation measures how strongly the system retains correlation with its past states over time. Specifically, its calculation is presented in Appendix I. In this plot, all cases exhibit a decay in autocorrelation, eventually showing no correlation with the initial state. The configuration with Q-Prior demonstrates stronger short-term correlation (the same as the ground truth data) compared to the model without Q-Prior, indicating better preservation of temporal dynamics in the early prediction period. These outcomes demonstrate that our designed Q-Prior can regularize the classical ML model, preserving both long-scale and small-scale structures, and improving long-term statistical accuracy.

## C. 2D Kolmogorov flow

Next, we apply our QIML framework to learn the dynamics of the 2D Kolmogorov flow, a canonical example of incompressible Navier-Stokes dynamics under sinusoidal forcing. The governing equations are:

$$\frac{\partial \mathbf{u}}{\partial t} + (\mathbf{u} \cdot \nabla)\mathbf{u} = -\nabla p + \nu \nabla^2 \mathbf{u} + \mathbf{F}, \tag{13}$$

$$\nabla \cdot \mathbf{u} = 0, \tag{14}$$

where  $\mathbf{u}$  is the velocity field, p represents the pressure. Here **u** denotes the velocity field on the 2D cases. In the algorithmic expressions, we revert to the simpler symbol u, using it as a generic placeholder for both 1D scalar and 2D velocities, since the learning procedure applies uniformly across dimensionalities.  $\nu$  is the kinematic viscosity, and the forcing term is given by  $\mathbf{F}(x,y) = (F\sin(ky),0)$  for some amplitude F and wave number k. The domain is periodic in both x and y directions:  $(x,y) \in [0,L_x] \times [0,L_y]$  with  $L_x = L_y = 64$  grids. The data source is presented in Appendix D. We use 80% for training, 10% for validation, and 10% for testing. For this system, both the classical Koopman machine learning (without Q-Prior) and the main QIML model (with Q-Prior) are trained for 500 epochs. For QIML, the quantum generator uses n=10 qubits ( $2^{10}=1024$ basis states) and 180 trainable parameters. Detailed network architectures, training hyperparameters, and data generation procedures are provided in Appendix G.

Fig. 3 presents the predicted streamwise velocity fields over a 20-step autoregressive rollout ( $t_{\rm window}=20$ ), where the time is normalized as  $\hat{t}=t/t_{\rm window}$ . The snapshots qualitatively demonstrate that the QIML model preserves the coherent vortical structures of the ground truth with higher fidelity and for a longer duration compared to its classical counterpart, in which these features decay more rapidly into a disorganized state. Fig. 4 reports the comparative performance of the baseline ML model (without Q-Prior) and the quantum-informed

ML model (with Q-Prior) on the two-dimensional Kolmogorov flow dataset. Panel (a) shows the time-averaged velocity field and the corresponding turbulent kinetic energy (TKE) field across three configurations: the ground truth from simulation, the classical model trained without Q-Prior, and the quantum-informed model trained with Q-Prior. All models are evaluated on the same test data. Both the "with Q-Prior" and "without Q-Prior" models perform auto-regressive (one frame in one frame out) inference over a horizon of  $t_{end} = 1000$  time steps. The visualizations span a two-dimensional domain of size  $64 \times 64$  in the x-y plane. The time-averaged velocity field is plotted in the left column, and the corresponding TKE field is shown in the right column. The ground truth velocity field (top left) exhibits coherent, stripelike structures, and its TKE field (top right) reveals concentrated regions of high energy, indicating the presence of organized flow features. The model without Q-Prior (middle row) shows degraded spatial coherence in the velocity field, with disrupted patterns and more noise-like structures. In contrast, the model with Q-Prior (bottom row) recovers a more organized velocity field, better preserving the stripe patterns observed in the ground truth. Its associated TKE field also aligns more closely with the ground truth. Panel (b) presents the ensembleaveraged energy spectrum  $\langle E(k) \rangle$  as a function of the wavenumber k for the raw data (solid blue line), the machine learning model without Q-Prior (green dashed line), and the model with Q-Prior (orange dash-dotted line). The spectrum from the model without Q-Prior overestimates the energy spectrum at low and intermediate wave numbers. However, the Q-Prior aligns closer to the raw data across the whole spectrum. Then, we further examine the overall velocity distributions. As illustrated in panel (c), we compare the predicted velocity probability density functions from both machine learning models. The raw data exhibit a sharply peaked distribution with heavy tails, characteristic of the system's inherent velocity fluctuations. Both machine learning models capture the general symmetric shape of the distribution, but tend to slightly underestimate the peak and overestimate the spread. Among them, the model with Q-Prior more closely matches the raw data, particularly around the peak and in the tails, indicating improved accuracy in reproducing the system's statistical behavior. This is quantitatively supported by a 6.57% reduction in the MSE for the Q-Prior model's predictions compared to the classical model without the prior over the first 100 steps. This advantage is particularly pronounced in the high-probability peak of the distribution (where |u| < 2), where the MSE reduction for the Q-prior model increases to 10.39%. On a global scale, this superior performance is also reflected in the energy spectrum, where the Q-Prior achieves a 14.16% MSE reduction. These results further support the conclusion that incorporating the Q-Prior enhances the machine learning model's ability to recover velocity statistics. We also examined the autocorrelation of the field over time. Panel (d) plots the autocorrelation

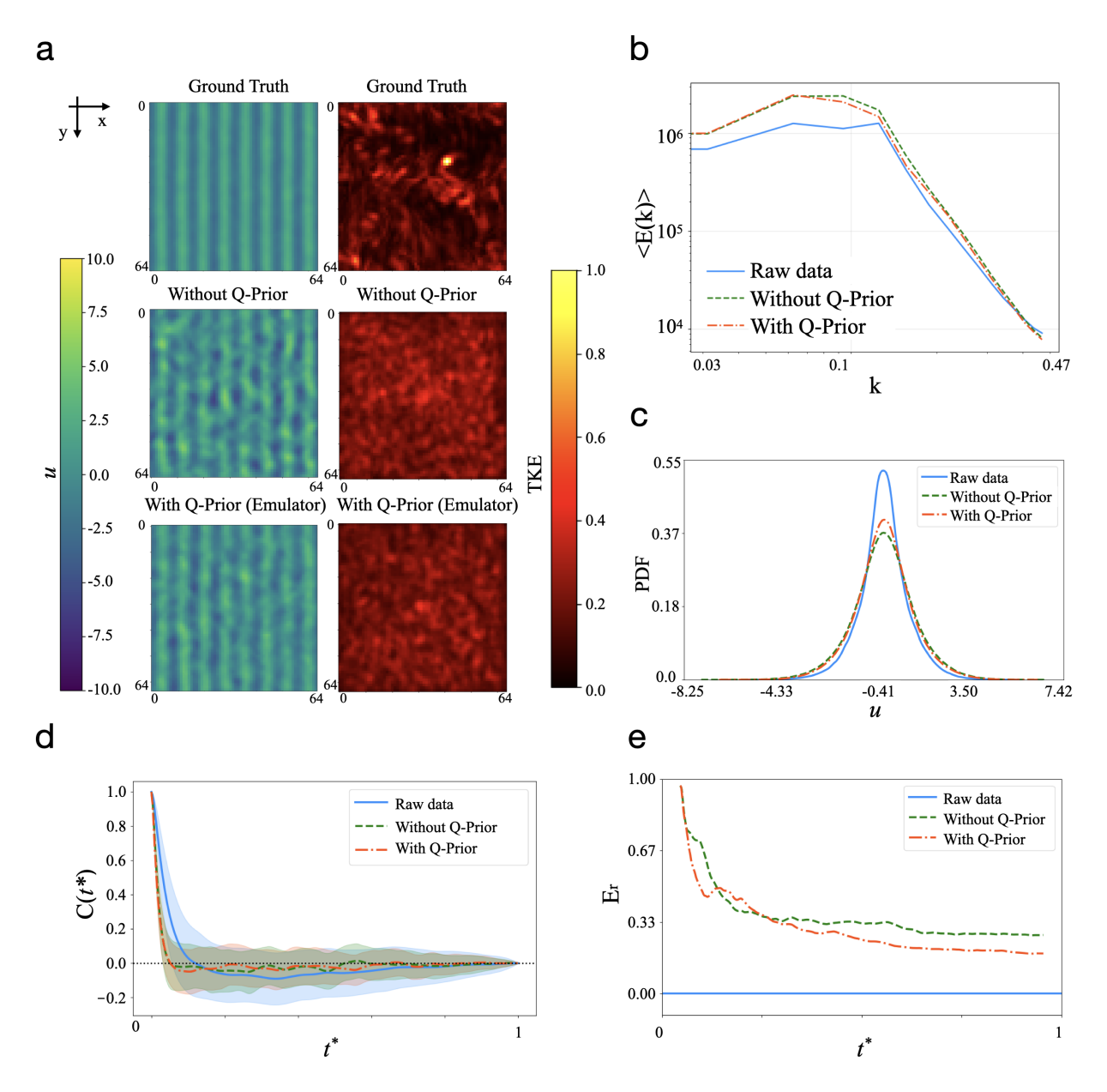


FIG. 4. Evaluation of the QIML framework on the 2D Kolmogorov flow. a. This panel displays time-averaged mean u fields (left column) and corresponding TKE fields (right column) for the ground truth, the classical model without Q-Prior, and the quantum-informed model with Q-Prior. These maps are evaluated on the test set, highlighting long-term flow patterns and energy distribution. b. This panel presents the ensemble-averaged energy spectrum  $\langle E(k) \rangle$  as a function of spatial wavenumber k. c. This panel shows the PDF of the field variable u, comparing the distribution from the raw test data with the PDFs predicted by the models with and without the Q-Prior. d. This panel plots the temporal autocorrelation  $C(t^*)$  of the velocity field as a function of dimensionless time  $t^*$ . e. This panel reports the normalized relative error,  $E_r$ , with respect to the ground truth, calculated over time on the same validation trajectory for a 1000-step rollout.

 $C(t^*)$  of the velocity field as a function of dimensionless time  $t^* = t/t_{end}$ . The correlation is computed over 100 randomly sampled locations, with shaded regions indicating one standard deviation. Both models reproduce long-term decay in autocorrelation followed by fluctuations around zero, consistent with the expected loss of memory in a chaotic or turbulent system. To further analyze the model, panel (e) reports the normalized relative auto-correlation error  $E_r$  with respect to the ground truth. The raw data serves as the reference baseline with zero error. The model without Q-Prior shows a gradual decrease in relative error over time but maintains a consistently higher error floor. In contrast, the model with Q-Prior exhibits a more rapid reduction in normalized relative error and achieves lower relative error throughout the prediction horizon.

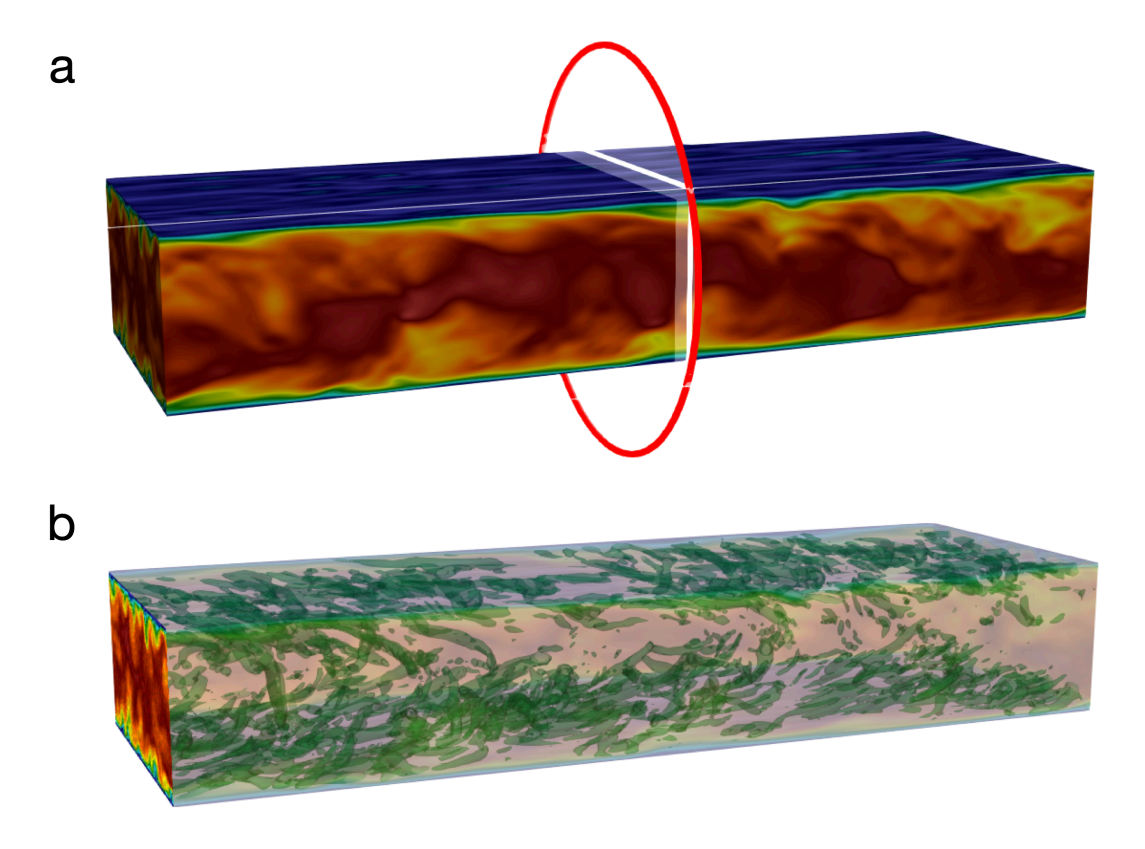


FIG. 5. Generation of Synthetic Turbulent Inflow from Turbulent Channel Flow Data. a. Instantaneous flow field from a turbulent channel flow simulation, representing the raw data used for turbulent inflow generation. The red ellipse indicates the cross-section where velocity field data are extracted. b. The QIML generative model can be used as turbulent inflow conditions in 3D turbulent channel flow for large eddy simulations.

These observations confirm that the quantum-informed Q-Prior can provide additional information that improves classical ML fidelity and velocity statistics, and enhances long-horizon accuracy.

## D. Turbulent channel flow inflow generation

We further evaluate our QIML framework on turbulent channel flow, a representative case of wall-bounded turbulence. In this setting, the training data is obtained from the mid-plane cross-section of a fully developed periodic turbulent channel flow at friction Reynolds number  $Re_{\tau} = 180$ . Note that the reference data has been validated with the DNS data [75] (See Appendix E). The reference data is generated using the LBM solver, which serves as an efficient alternative to directly solving the Navier-Stokes equations [74, 76]. A large eddy simulation (LES) formulation is employed to capture the largescale turbulent structures [24, 77]. Figure 5 a shows the instantaneous velocity field extracted from the highfidelity turbulent channel flow simulation, with the red ellipse marking the cross-section used as the source data for inflow synthesis. The governing equations used for generating the data are provided in Appendix E. The

detailed description of the data generation setup is in Appendix H. The channel flow snapshots are split 80:10:10 into training, validation, and test sets. For this system, both the classical Koopman machine learning model (without Q-Prior) and the main QIML model (with Q-Prior) are trained for 500 epochs. For QIML, we employ a 15-qubit quantum generator ( $2^{15}=32\,768$  basis states) with 240 trainable parameters. Detailed network architectures, training hyperparameters, and data generation procedures are provided in Appendix G. Figure 5 b depicts the corresponding synthetic turbulent inflow generated by the QIML model, demonstrating its capability to produce physically consistent inflow conditions for large-eddy simulations [77].

Figure 6 presents the evaluation of the quantum-informed machine learning framework on the turbulent channel flow dataset. Our ML models perform autoregressive (one frame in one frame out) inference over a horizon of  $t_{end}=1000$  time steps. The visualizations span a two-dimensional domain of size  $64\times64$  in the x-y plane. Panel (a) shows a comparison of time-averaged velocity magnitudes u across a  $64\times64$  domain for the ground truth, the machine learning model without Q-Prior, and two Q-Prior-enhanced variants: the emulator and real superconducting IQM device. The colorbar on

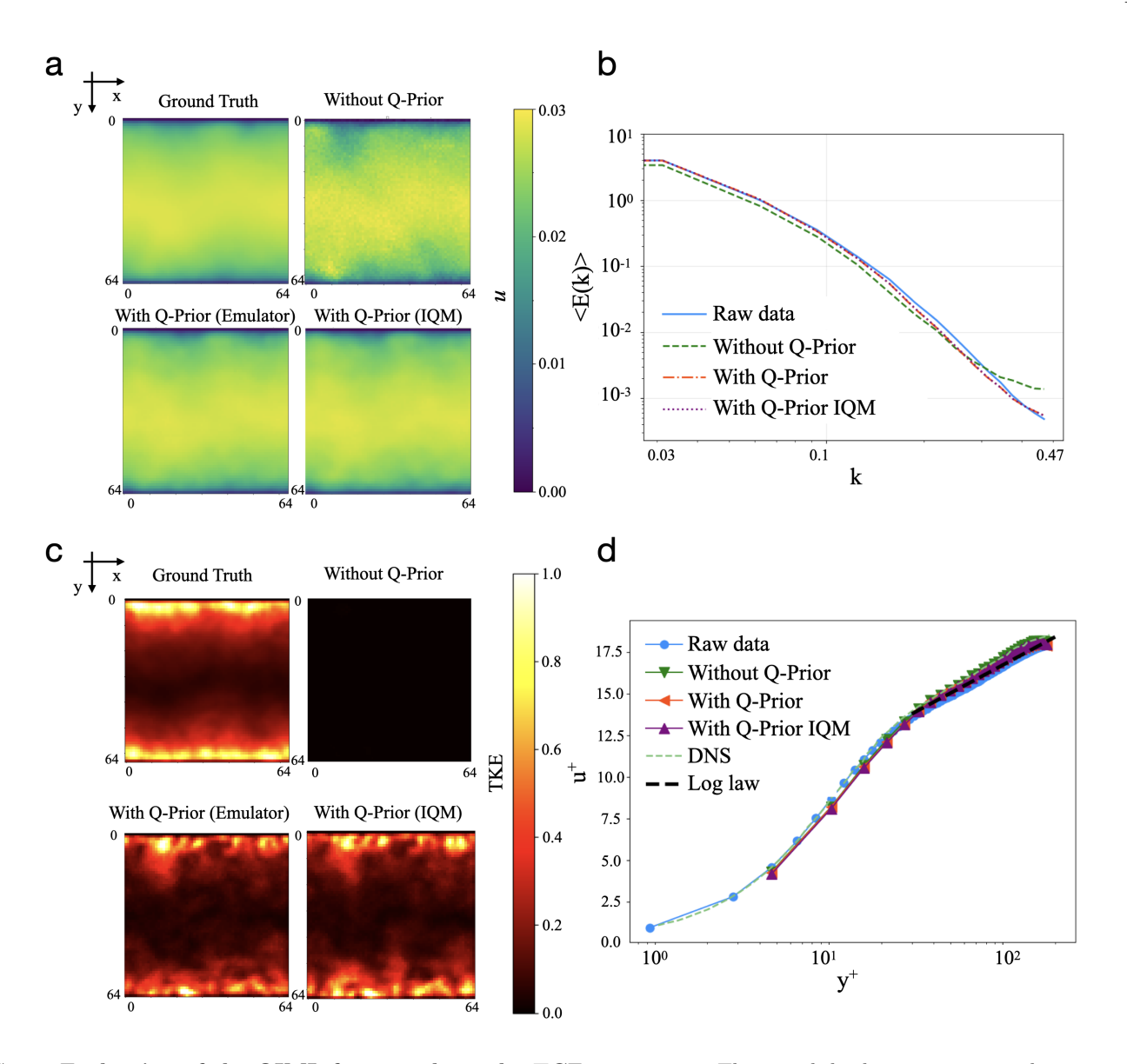


FIG. 6. Evaluation of the QIML framework on the TCF system. a. This panel displays time-averaged streamwise velocity fields across different models. Each row corresponds to a different model output: the top row displays the ground truth obtained from DNS, followed by results from the classical model without Q-Prior, the QIML model using Q-Prior trained on the emulator, and the model using a Q-Prior trained on real superconducting hardware (IQM). b. This panel plots the ensemble energy spectrum  $\langle E(k) \rangle$  as a function of the spatial wavenumber k. c. This panel displays the time-averaged TKE field for the same four configurations as in panel (a), using a normalized color scale to enhance visual comparability. d. This panel shows the non-dimensional velocity profile  $u^+$  as a function of the wall-normal coordinate  $y^+$  on a logarithmic scale. Results are compared with the empirical log-law and DNS reference, using the same validation data as in previous panels.

the right indicates the magnitude of u, with higher values in yellow and lower values in blue. The ground truth (top left) displays smooth, large-scale variations in the velocity field. The model without Q-Prior (top right) introduces noticeable small-scale noise and fails to capture the smooth gradients seen in the true field. In contrast, both Q-Prior (with emulator and with IQM device) models (bottom row) closely match the ground truth, preserving the dominant spatial structures and exhibiting lower spurious variability. Panel (b) plots the ensemble energy spectrum  $\langle E(k) \rangle$  as a function of the wavenumber

k for the raw data (solid blue line), the machine learning model without Q-Prior (green dashed line), the model with Q-Prior (orange dash-dotted line), and the model with Q-Prior IQM (purple dotted line). The model without Q-Prior deviates from the ground truth at higher wavenumbers, with discrepancies arising at smaller spatial scales, which indicating a failure to capture the essential small-scale physical dynamics of the system. As we will demonstrate in the following section IV, this is a common failure mode for state-of-the-art classical architectures. In contrast, both Q-Prior variants better cap

ture the energy distribution across all scales. Panel (c) compares the normalized TKE fields across a  $64 \times 64$ spatial domain for the ground truth, the model without Q-Prior, and two Q-Prior-based configurations: the emulator and IQM. The ground truth (top left) displays spatially structured regions of elevated TKE, particularly near the domain boundaries, reflecting characteristic flow features. The model without Q-Prior (top right) fails to capture any meaningful TKE patterns, instead producing a near-zero field, which indicates an almost static prediction over time. In contrast, both Q-Prior-based models (bottom row) recover structured TKE fields that closely resemble the ground truth. These models preserve the dominant energy distribution and capture the spatial organization of turbulent structures more accurately. Panel (d) shows the dimensionless velocity profile  $u^+$  as a function of the dimensionless wall-normal coordinate  $y^+$ . Our results are compared with the raw data, log-law and DNS reference. All machine learning models reproduce the canonical log-law behavior and match well with the reference data, DNS data and log law.

Overall, the Q-Prior provides a clear improvement in the spatiotemporal prediction of cross-sections in turbulent channel flow, where governing equations for the cross-sectional dynamics are not explicitly defined. This makes it a potentially valuable tool for engineering applications that rely on coupling Reynolds-Averaged Navier–Stokes (RANS) and LES approaches [77].

Collectively, these results demonstrate that embedding Q-Priors significantly improves long-term prediction results and statistical alignment of classic machine learning models in high-dimensional dynamical systems. Even with modest quantum resources, that is, no more than 15 qubits and under 300 parameters (specifically shown in method F, Appendix B), our framework captures essential dynamics of high-dimensional flows and enables practical hybrid learning pipelines for scientific applications. By anchoring predictions to Q-Prior, the QIML model improves statistical fidelity and stability, laying the groundwork for practical quantum—classical synergies in the modeling of turbulent and other chaotic physical systems.

## IV. COMPARATIVE ANALYSIS OF QIML AGAINST MACHINE LEARNING BASELINES

To rigorously quantify the contribution of our quantum-informed machine learning framework, we conduct a comparative analysis of our full QIML architecture against key baseline models. The aim is to show that the stability and statistical fidelity observed in our results arise from the Q-Prior guidance, rather than being solely attributable to the autoregressive classical ML model's architecture. Both the QIML framework and the classical baselines are trained on exactly the same raw dataset. The fundamental difference lies in the architectural approach instead of unequal access to data.

Here, we consider two primary classes of baselines: (i) a classical state-of-the-art Koopman-based autoregressive machine learning model trained without the Q-Prior, and (ii) neural operators for nonlinear PDEs and chaotic systems such as the Fourier neural operator and the Markov neural operator [78].

As demonstrated in Fig. 7, our classical model without the Q-Prior consistently fails to maintain long-term stability. While capable of accurate short-term predictions, it inevitably succumbs to error accumulation, leading to prediction divergence and a failure to reproduce the system's invariant statistical measures. The comparison with neural operators provides a more stringent test. FNOs and MNOs are known for their strong performance in learning resolution-independent solutions to nonlinear PDEs and chaotic systems. We trained both models on the same datasets used for our framework. We observed that for short-term predictions, their accuracy is competitive. However, when tasked with long-horizon autoregressive rollouts, the classical Koopman-based machine learning model, the FNO and MNO models exhibit the same fundamental weakness: a gradual divergence from the ground truth and a failure to preserve the correct spatio-temporal evolution of the chaotic system. This failure is particularly striking given their substantial size; both the FNO and MNO models employ an order of magnitude more trainable parameters than our QIML framework, as detailed in the comparison in the Table III.

This comparative analysis leads to a clear conclusion: the key enabling component of our framework is the Q-Prior integrated into the machine learning. The long-term instability is a fundamental challenge for even powerful classical architectures like FNOs and MNOs. By providing a physically grounded, memory-efficient statistical regularizer, the Q-Prior confers the necessary stability and long-term fidelity that are otherwise absent. This result underscores the unique and practical advantage of our QIML architecture.

## V. Q-PRIOR MEMORY EFFICIENCY

A defining feature of the proposed framework is its capacity to extract high-dimensional physical information using significantly fewer trainable parameters than conventional deep learning models. The Q-Prior, operating on only 10-15 qubits and comprising fewer than 300 trainable parameters, successfully captures invariant distributions over spatial domains with dimensionality exceeding 10<sup>4</sup>. In contrast, a classical neural network capable of learning an equally expressive distribution over the same domain would require at least  $\mathcal{O}(10^4)$  parameters, assuming a minimal fully connected architecture with comparable granularity. For example, on a grid of  $D = 2^{10} = 1,024$  spatial points, the lightest fully-connected (FC) network that can approximate an arbitrary probability map with standard universal-approximation accuracy must allocate  $\mathcal{O}(D^2)$ 

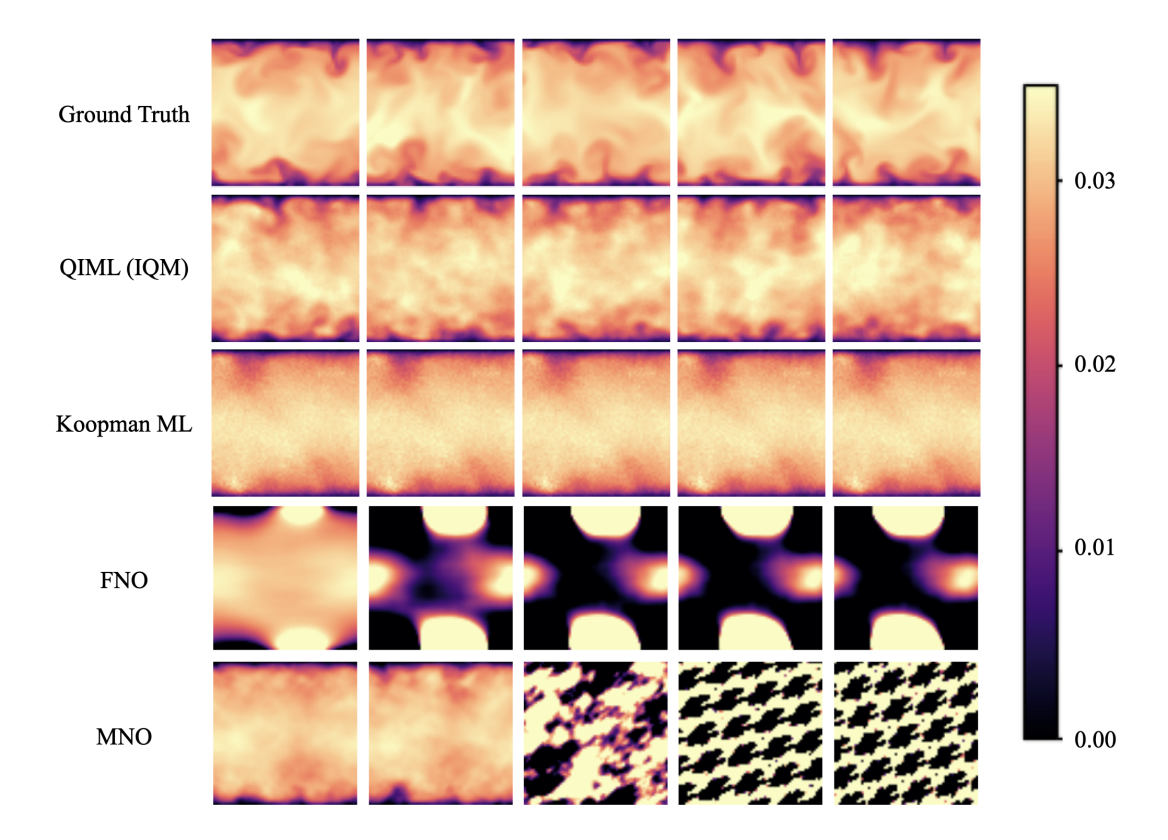


FIG. 7. Qualitative comparison of long-term autoregressive predictions for the turbulent channel inflow. Snapshots of the velocity field are shown at representative predictive time steps t=20,40,60,80, and 100 (from left to right) for the Ground Truth and for predictions from the QIML (IQM), classical Koopman ML, FNO, and MNO models. The comparison highlights the superior performance of the QIML, which is the only method to maintain structural fidelity with the ground truth, whereas the classical baselines either collapse to an overly smooth, time-averaged field or diverge into non-physical artifacts.

weights [79, 80]. Even with an aggressively thinned hidden layer, this still amounts to  $\sim 2.5 \times 10^5$  tunable parameters—three orders of magnitude more than the 300 parameters used by our ten-qubit Q-Prior (see Appendix B). Moreover, classical models lack access to quantum entanglement, limiting their ability to compactly encode non-local correlations and higher-order statistical dependencies prevalent in turbulent or chaotic systems.

However, possessing a parameter-efficient quantum representation is only the first step; leveraging it to guide a classical machine learning model is a distinct and significant challenge. We address this by designing a composite loss function that seamlessly integrates the statistical information from the Q-Prior into the classical model's training process. This enables a true "quantum-informed" learning paradigm where the quantum component actively regularizes the classical dynamics, leading to superior results as demonstrated in this work. As shown in the Table I, the successful implementation of this hybrid integration unlocks a further, highly practical potential of quantum computing: memory efficiency in data storage and transfer.

Specifically, for the turbulent–channel dataset, retaining all mid-plane snapshots in double precision requires roughly  $5.0 \times 10^2$  MB. Archiving the corresponding Q-

Prior checkpoint for each snapshot (4.3 kB per file) occupies only  $595 \times 4.3$  kB  $\approx 2.5$  MB, a compression greater than two orders of magnitude while preserving the relevant flow statistics. Comparable savings are obtained for Kolmogorov flow ( $\sim 180$  parameters,  $\sim 1.4$  kB per file,  $\sim 0.44$  MB in total) and Kuramoto–Sivashinsky data ( $\sim 120$  parameters,  $\sim 1$  kB per file,  $\sim 1.4$  MB in total). Full storage calculations are shown and reported in Appendix H. Such dramatic savings make the Q-Prior attractive whenever data are expensive to generate or archive, while still providing a statistically faithful, low-parameter regularizer for the classical Koopman machine learning.

Crucially, this provides a blueprint for future hybrid computing infrastructures where the quantum processors might be co-located with every classical computer. Instead of transferring voluminous raw datasets, which can amount to hundreds of gigabytes or more, one would only need to transfer the compact Q-Prior. As our results show, this corresponds to a data storage reduction of over two orders of magnitude. Furthermore, this vision is made practical by a key finding that directly addresses the number of measurement shots, a widely scrutinized issue for NISQ-era algorithms. While the results presented in this work are based on a high shot count

(20,000 per iteration) to demonstrate the framework's maximum potential, we found that the classical model does not require a perfectly resolved, exponentially large distribution to be effective. In fact, reducing the measurement count to 8,000 shots had a negligible impact (less than 5%) on the final model's performance, showing that an approximate prior is sufficient to act as a powerful guiding signal. Crucially, the Q-Prior is trained only once in an offline stage, rather than being re-evaluated during every rollout or trained iteratively within the ML framework like QEML. This one-time training greatly reduces the overall computational burden and differentiates our approach from iterative hybrid quantum-classical schemes that require repeated quantum calls throughout the learning process. Thus, QIML establishes a viable and economically attractive framework: a central, highfidelity quantum processor performs the intensive, onetime training of a master Q-Prior, whose compact parameters are then distributed at low cost to remote systems. This paradigm may serve as a template for future cloud quantum platforms, where the quantum processors provide powerful statistical guidance and data support for large-scale classical models.

TABLE I. Quantum resources and storage compression achieved by the Q-Prior.

Dynamical System	Raw data (full set)		Compression (ratio)
Kuramoto-Sivashinsky	$300~\mathrm{MB}$	$0.25~\mathrm{MB}$	$\approx 1.2 \times 10^3 : 1$
2D Kolmogorov flow	$400~\mathrm{MB}$	$0.40~\mathrm{MB}$	$\approx 10^3:1$
Turbulent channel flow	500  MB	$2.3~\mathrm{MB}$	$\approx 2.2 \times 10^2 : 1$

# VI. ON THE NATURE OF QUANTUM "ADVANTAGE" IN QIML

The term "quantum advantage" must be approached with caution, particularly in the context of quantum computing and quantum machine learning [65, 81]. As recent analyses have highlighted, many claims of quantum advantage are later matched or surpassed by sophisticated classical algorithms, revealing that the initial gap was due to the immaturity of classical methods rather than a fundamental quantum superiority [65]. We have deliberately refrained from prominently using this term because of its ambiguity. With the exception of algorithms like Shor's [82], which leverage the fundamental nature of quantum mechanics in a provably superior way, many claims of advantage are eventually challenged. Even powerful algorithms such as the Harrow-Hassidim-Lloyd (HHL) algorithm have faced scrutiny [83], with new classical works emerging that achieve comparable performance in specific contexts [65]. Here, we do not assert that QIML holds an unassailable advantage. Instead, we posit that its effectiveness stems from a foundational quantum principle that, in this application, has not been

classically replicated.

The foundational advantage exploited by our Q-Prior stems from the ability of an n-qubit quantum state to represent a classical vector in a  $2^n$  dimensional space, which is considered as a genuine quantum advantage [67]. This provides an exponential advantage in information storage capacity. This type of advantage has found recent applications in quantum machine learning, such as for computing quadratic functions of data [84]. However, this potential is famously constrained by Holevo's bound, which dictates that only O(n) classical bits of information can be reliably extracted from an n-qubit state through measurement [85]. If full reconstruction of the classical information were required, the need for an exponential number of measurements would negate the storage advantage entirely.

In ergodic theory, the invariant measure governs the long-time statistical behavior of chaotic dynamics, even though individual trajectories diverge exponentially [86]. The central insight of the QIML framework is to circumvent Holevo's bound by extracting only this essential invariant measure without reconstructing the full dataset, yielding a compressed yet sufficient representation of the system. This low-dimensional representation is precisely what is needed to regularize the classical ML, guiding it away from non-physical trajectories without needing to know every detail of the system's state. Therefore, the advantage demonstrated here is a representational and memory advantage that translates directly into a performance advantage.

Memory Efficiency: The Q-Prior leverages quantum entanglement to capture complex, non-local correlations within the invariant measure using a few parameters. This translates to a dramatic, orders-of-magnitude reduction in data storage, as quantified in Table I.

**Performance Gain:** This compact and physically rich representation provides the crucial regularization that leads to long-horizon stability and statistical fidelity, a task at which larger, more complex classical models like FNO and MNO demonstrably fail for this class of problems.

While it is an open question whether other classical models could be adapted to leverage the Q-Prior as effectively, our results suggest that the co-design of the hybrid architecture is key. We anticipate that our results may inspire new classical approaches. For instance, using large generative models to learn the invariant measure, that could achieve comparable predictive performance. However, we argue that such methods are unlikely to replicate the foundational source of the advantage demonstrated here: the physical ability to logarithmically compress high-dimensional data and extract the necessary guiding information without an exponential measurement cost. This is possible because the invariant measure appears to be a sufficiently rich representation of the essential physics of chaos. Capturing its key features provides the necessary guidance to unlock the observed gains in performance and, crucially, in memory efficiency. This efficiency is a direct, physical consequence of the quantum representation, and while our theoretical understanding of the measure's precise role is still developing, the empirical results provide compelling evidence for this paradigm's value.

Another notable point is that much of that research begins with a search for theoretical advantage, often struggling to connect with practical, "useful" applications [65]. In contrast, our investigation was born from a practical necessity: to solve the long-horizon prediction problem for chaotic systems, where leading classical methods fail. By showing that a 10-qubit quantum device can provide a unique resource, this work provides a compelling example of a useful quantum "advantage" and motivates the further development of both quantum and classical algorithms for scientific machine learning.

## VII. IMMEDIATE AND FUTURE IMPACT OF QIML

To reduce the impact of hardware noise and enable stable training, the quantum generator is optimized separately and remains fixed during the training of the classical model. This architectural constraint arises from the limited scalability and noise of NISQ superconducting devices, which make full end-to-end quantum training infeasible at present. For near-term work, further improvements are possible within this offline training paradigm. While current Q-Priors are limited by qubit count, circuit depth, and hardware noise, deeper architectures with structured entanglement (e.g. hardwareefficient ansätze) may further improve expressivity for highly anisotropic distributions. Besides, while this work demonstrates improvements in learning from digitally generated high-dimensional dynamical system data, we acknowledge the inherent limitations of the digital computing part of our method in fully capturing the true continuum behavior of high-dimensional dynamical systems [5–8]. Our ground truth here is, by definition, a 64-bit floating-point approximation. Future work will explore the use of analogue computation to provide a more direct comparison with the true invariant measures, thus offering a more rigorous validation of our approach against the ultimate ground truth.

Although there are limitations from NISQ hardware, in contrast to prevailing scepticism about the immediate applicability of quantum learning algorithms [36, 81], QIML demonstrates that even current quantum devices can contribute meaningfully to the modeling of high-dimensional dynamical systems. Without resorting to fault-tolerant hardware, lightweight NISQ-based quantum modules enhance classical machine learning models by providing data-driven Q-Priors that efficiently capture complex statistical structures and non-local correlations—features that are otherwise challenging for classical methods to acquire with comparable memory efficiency. The resulting gains in statistical fidelity and

long-horizon stability, coupled with a substantial reduction in data storage requirements, point to an immediate and practical role for near-term quantum resources in scientific machine learning. The compact 10- to 15-qubit Q-Prior presented here exemplifies how such modules can be effectively integrated today.

Looking forward, the QIML architecture introduced here serves as an intermediate but essential step toward fully realizing quantum machine learning pipelines. While our current framework integrates quantum priors into classical machine learning models, we envision future extensions in which quantum circuits not only generate priors but also perform end-to-end learning and generation for high-dimensional datasets. Given the exponentially larger Hilbert space accessible to quantum systems, such models are expected to possess superior expressivity for learning high-dimensional generative tasks.

Furthermore, this work opens up more exciting avenues for future research. A key question is how the framework performs with sparse or partial datasets, a common scenario in real-world applications where obtaining a complete ground-truth solution is impossible. Our current results are already promising in this regard, as the Q-Priors were successfully trained using only a subset of the available data (see section III) while still providing effective guidance. This suggests the potential for a more profound, out-of-distribution generalization [87]. For instance, future work could explore whether a single Q-Prior, trained on the invariant measure of one system, could successfully regularize a model for a different system that shares similar statistical properties but has different underlying dynamics. The successful demonstration of such a "universal" prior would have significant implications, potentially allowing one Q-Prior to guide multiple machine learning models, further enhancing the practical value and efficiency of the QIML paradigm.

As quantum hardware continues to advance, in terms of qubit count, coherence time, and error mitigation, the prospect of replacing classical generative backbones with fully quantum circuits becomes increasingly viable. Also, this hybrid architecture lays the groundwork for a future paradigm of highly efficient information transfer within large-scale infrastructures. As quantum devices advance, one can envision a scenario where highly compressed Q-Priors, containing essential physical statistics, are transferred between compute nodes in place of voluminous classical datasets, which are riddled with spurious correlations [88]. This mechanism offers a scalable solution for future large-data training and provides a foundation for progressively more capable quantum-native machine learning models as the hardware matures. Thus, the parameter and memory efficiency demonstrated in this work suggest a pathway for Q-Priors to ultimately influence entire sections of large classical models.

#### VIII. CONCLUSION

This paper introduces a practical, scalable quantum-informed approach to a critical challenge in scientific machine learning: achieving stable, long-horizon autoregressive predictions for high-dimensional, nonlinear systems. We redefine the division of labor—using the quantum computer not for speed, but to learn a compressed statistical model of the underlying physics that guides a classical model to maintain fidelity where it would otherwise struggle.

In QIML, a sample-based quantum generator is trained once, offline, to learn invariant statistical properties from high-dimensional flow data. The resulting compact Q-Prior is integrated as a global statistical constraint within a classical ML model. We validate QIML on three representative high-dimensional systems, showing consistent gains in stability and fidelity over classical baselines. These gains across qualitatively distinct systems demonstrate strong generalization to other nonlinear dynamical problems. In the most challenging turbulent channel flow case, state-of-the-art models such as FNO and MNO fail to sustain stable rollouts and diverge from correct statistics, whereas QIML maintains stability and accurately learns invariant measures of complex physical systems.

Another contribution of this work is its demonstration of parameter efficiency and memory advantage. Using fewer than 300 trainable parameters, the quantum generator, trained once and offline, captures statistical distributions over a state space exceeding 30,000 dimensions. This efficiency stems from the Q-Prior's exploration of a high-dimensional Hilbert space, enabling it to learn long-range velocity correlations. Unlike many QEML approaches that require expensive, iterative quantum-classical training loops and costly data embedding, our offline-trained Q-Prior can be reused without further quantum hardware access. On the TCF dataset, QIML maintains predictive stability while using an order of magnitude fewer trainable parameters in the machine learning model and reducing storage and data transfer costs by over two orders of magnitude, all without sacrificing performance. This capability opens a scalable pathway for applying quantum-informed machine learning to domains where reliable prediction of highdimensional, chaotic systems can unlock new scientific insights and enable practical engineering solutions.

## IX. DATA AVAILABILITY

All data needed to evaluate the conclusions in the paper are present in the paper and/or Appendix D. The training/validation/testing datasets for all three cases are available on https://doi.org/10.5281/zenodo.16419085.

#### X. CODE AVAILABILITY

The complete training code for the quantum generator module and the Koopman machine learning model is openly available at https://github.com/UCL-CCS/QIML.git.

#### XI. ACKNOWLEDGEMENTS

We would like to thank Professor Igor Mezic for his valuable comments on an earlier version of this paper. and Dr. Marcello Benedetti for his valuable feedback. We are also grateful to Thomas M. Bickley and Angus Mingare for their careful reading of the manuscript and insightful comments. We acknowledge funding support from the European Commission CompBioMed Centre of Excellence (Grant No. 675451 and 823712). Support from the UK Engineering and Physical Sciences Research Council under the projects "UK Consortium on Mesoscale Engineering Sciences (UKCOMES)" (Grant No. EP/R029598/1) and "Software Environment for Actionable and VVUQ-evaluated Exascale Applications (SEAVEA)" (Grant No. EP/W007711/1) is gratefully acknowledged. 2024-2025 DOE INCITE award for computational resources on supercomputers at the Oak and Argonne Leadership Computing Facility under the "COMPBIO3" project. We also gratefully acknowledge IQM Quantum Computers for providing access to superconducting quantum processors used in hardware benchmarking, and the Leibniz Supercomputing Centre (LRZ) for access to the BEAST GPU cluster, which supported the training of classical models and quantum circuit simulations.

#### XII. CONTRIBUTIONS

M.W. and X.X. jointly conceived the central idea of the study and collaboratively designed the quantuminformed machine learning framework. Both authors conducted the quantum hardware experiments and contributed equally to the classical modeling and validation. M.G. performed the numerical simulations for the machine learning baselines and curated the results for the comparative analysis. M.W. led the writing of the quantum algorithm and hardware implementation sections, while X.X. was responsible for drafting the classical modeling and chaotic system descriptions. Data analysis, hyperparameter tuning, and visualization were carried out jointly by M.W. and X.X. P.V.C. provided guidance throughout the evolution of the project, including software and hardware execution and optimization processes. All authors discussed the results and contributed to the overall manuscript.

## Appendix A: Quantum Computing and Quantum Generator

## 1. Quantum Computing

Quantum computing operates on the principles of quantum mechanics, allowing for a novel class of information processing paradigms. The fundamental unit of quantum information is the *qubit*, which exists in a superposition of classical states. Formally, a single qubit can be represented as

$$|\psi\rangle = \alpha|0\rangle + \beta|1\rangle,\tag{A1}$$

where  $\alpha, \beta \in \mathbb{C}$  and  $|\alpha|^2 + |\beta|^2 = 1$ . Upon measurement in the computational basis, the qubit collapses to state  $|0\rangle$  or  $|1\rangle$  with probabilities  $|\alpha|^2$  and  $|\beta|^2$ , respectively. In an *n*-qubit system, the global state resides in a  $2^n$ -dimensional Hilbert space, allowing the compact representation of complex, high-dimensional distributions.

## 2. Quantum Machine Learning

Recent progress in quantum computing has spurred the rapid emergence of quantum machine learning (QML) as a promising interdisciplinary field at the intersection of quantum information science and statistical learning. QML algorithms are designed to exploit quantum phenomena, such as entanglement, interference, and superposition, to augment learning efficiency or representational capacity in ways that may surpass traditional counterparts. A variety of model classes have been developed within this paradigm, including quantum autoencoders [89–91], which perform lossy compression and denoising on quantum data using a reduced number of qubits, and quantum Boltzmann machines [92, 93], which offer a framework for generative modeling and state tomography through quantum sampling of thermal distributions.

Another line of work explores quantum generative adversarial networks (QGANs) [45, 94, 95], which have been employed to emulate quantum systems and approximate entangled states through adversarial training mechanisms. In the context of supervised learning, quantum kernel methods [96–98] have been proposed to enhance the expressive power of traditional classifiers by mapping data into high-dimensional Hilbert spaces via quantum feature maps.

Despite the theoretical potential of QML models, their application to real-world, non-quantum datasets remains in its infancy. Many benchmark results have been demonstrated, primarily in controlled settings with synthetic or quantum-native inputs. Notably, Huang et al. [67] recently showed that a 40-qubit quantum processor could infer global properties of a data distribution using exponentially fewer samples than traditional learners, albeit in a tightly constrained regime. While such results mark a significant step forward, the challenge of applying QML to traditional scientific tasks with high-dimensional structure and dynamical complexity remains open.

Such matters motivate us to develop a quantum-informed machine learning framework (QIML) that incorporates quantum components as functional modules within traditional workflows. In particular, demonstrating the ability of QML models to learn nontrivial statistical priors or invariant structures from real data, such as those arising in fluid dynamics or nonlinear PDEs, would provide a critical proof-of-concept for their practical relevance. To this end, and to circumvent the significant challenge of encoding high-dimensional classical data into quantum states, our QIML framework utilizes a sample-based quantum circuit as its generative module.

## 3. Sample-based Quantum Generator

Quantum generative models have shown great potential recently [99, 100], where quantum circuits are trained to learn quantum states or model traditional probability distributions. The quantum generator employed in this work is a sample-based model, with an architecture based on the quantum circuit Born machine. Given a parameterized quantum circuit  $U(\theta)$ , initialized from the all-zero state  $|0\rangle^{\otimes n}$ , the probability of observing a bitstring  $x \in \{0,1\}^n$  upon measurement is governed by the Born rule:

$$p_{\boldsymbol{\theta}}(x) = |\langle x|U(\boldsymbol{\theta})|0\rangle^{\otimes n}|^2. \tag{A2}$$

These probabilities define an implicit generative model from which samples can be drawn directly via quantum measurement, without requiring explicit likelihoods or tractable gradients.

Quantum generators have demonstrated utility in modeling structured datasets in domains such as quantum chemistry, generative learning, and combinatorial optimization. However, their application to traditional physical systems, particularly those governed by nonlinear PDEs, remains limited. This is despite the deep structural parallels between quantum mechanics and classical dynamical systems: both evolve within high-dimensional Hilbert spaces,

exhibit conservation laws, and are constrained by symmetry principles. These analogies motivate the integration of quantum-generated priors into classical scientific machine learning pipelines.

The sample-based quantum generator implementation in this work is distinguished by its likelihood-free training approach: a parameterized quantum circuit encodes a probability distribution through measurement statistics, without ever writing down an explicit probability mass function. We describe the full circuit ansatz and its Born-rule output distribution in Methods C; the Appendix material therefore omits the detailed equations and simply points readers to that section for implementation specifics.

**Empirical and model sample sets.** A batch of empirical samples  $\{x_i\}_{i=1}^N$  is obtained by converting the normalized velocity magnitudes  $v(\mathbf{r})$  into a categorical distribution over spatial indices and drawing N indices. Model samples  $\{\tilde{x}_j\}_{j=1}^M \sim p_{\theta}$  are produced by executing the circuit M times on the quantum processor. These two finite sample sets constitute the sole inputs to the training loss.

**MMD training objective.** Using a characteristic kernel  $k(x, x') = \langle \phi(x), \phi(x') \rangle$  the maximum-mean-discrepancy (MMD) between the empirical and model samples is

$$\mathcal{L}_{\text{MMD}}(\boldsymbol{\theta}) = \frac{1}{N(N-1)} \sum_{i \neq i'} k(x_i, x_{i'}) + \frac{1}{M(M-1)} \sum_{j \neq j'} k(\tilde{x}_j, \tilde{x}_{j'}) - \frac{2}{NM} \sum_{i,j} k(x_i, \tilde{x}_j), \tag{A3}$$

which vanishes if and only if  $p_{\theta}$  matches the empirical distribution (N denotes the size of the empirical sample set  $\{x_i\}$  and M denotes the size of the model sample set  $\{\tilde{x}_j\}$ ). The loss depends solely on kernel evaluations of finite samples and therefore requires no closed-form density—an essential feature in high-dimensional chaotic flows.

**Parameter-update strategy.** On hardware, we employ a mixed optimization scheme. When analytic or simulator-based gradients are available (e.g. during pre-training), we use BFGS [71] or Adam [72]; on a noisy quantum processor, we switch to derivative-free methods such as COBYLA [73] or BFGS. In both cases, a mini-batch of M circuit samples is generated per update, with 20 000 shots and M3 read-out mitigation (see Section S2.2) to suppress measurement noise on the quantum hardware.

Why the quantum generator is efficient in this setting. With 10 or 15 qubits, the Hilbert space already spans  $2^{10} = 1024$  or  $2^{15} = 32\,768$  computational basis states—matching the spatial resolution of our coarsest flow field. Entanglement permits the implicit encoding of multi-point velocity correlations without enumerating them explicitly; the sample-based MMD objective circumvents intractable likelihoods and normalisation constants; and the adopted optimization schemes require only additional forward shots, avoiding ancillary qubits or deep state tomography. These properties allow the quantum generator to provide an informative, low-parameter prior that complements the classical Koopman machine learning model discussed in the main text.

In this study, we propose a hybrid quantum–classical architecture in which quantum generators are trained to learn invariant velocity distributions that characterise the long-term statistical structure of chaotic fluid systems. These learned quantum distributions serve as data-driven priors to regularize the predictions of a classical machine learning model trained on PDE dynamics. Specifically, let  $p_{\theta}(x)$  denote the generated prior distribution and  $\hat{q}(x)$  the empirical velocity distribution obtained from the prediction. We design a composite regularization strategy combining both a Kullback–Leibler (KL) divergence loss and an MMD loss:

$$\mathcal{L}_{KL} = D_{KL} \left( \hat{q}(x) \| p_{\theta}(x) \right), \tag{A4}$$

$$\mathcal{L}_{\text{MMD}} = \left\| \mathbb{E}_{x \sim \hat{q}(x)} [\phi(x)] - \mathbb{E}_{x \sim p_{\theta}(x)} [\phi(x)] \right\|_{\mathcal{H}}^{2}. \tag{A5}$$

Here,  $\phi(x)$  denotes a feature mapping into a reproducing kernel Hilbert space  $\mathcal{H}$ , and  $\hat{q}(x)$  is derived from the predicted velocity field. The KL term in equation (A4) captures first-order alignment between predicted and reference distributions in information-theoretic terms, while the MMD term measures higher-order statistical discrepancies under a kernel embedding. This dual-objective regularization is inspired by recent developments in physics-informed learning frameworks such as DysLIM [35], which have shown improved robustness in chaotic and high-dimensional regimes.

The total training objective combines the standard reconstruction loss with these quantum-informed priors:

$$\mathcal{L}_{\text{total}} = \mathcal{L}_{\text{recon}} + \lambda_{\text{KL}} \mathcal{L}_{\text{KL}} + \lambda_{\text{MMD}} \mathcal{L}_{\text{MMD}}, \tag{A6}$$

where  $\mathcal{L}_{\text{recon}} = \|\hat{u}_{t+1} - u_{t+1}\|^2$  and the hyperparameters  $\lambda_{\text{KL}}, \lambda_{\text{MMD}}$  are selected empirically to balance fidelity and long-term physical consistency.

By anchoring machine learning model predictions to quantum-learned invariant structures, the framework improves stability during roll-out and reduces drift caused by chaotic sensitivity. The quantum modules are implemented using 10-15 qubits and 3-8 layers of parameterized gates, with a total of 30-300 trainable parameters. Execution is

performed on the IQM Garnet superconducting quantum processor—a 20-qubit near-term quantum device with gate fidelities reported in [69] and Table II. Circuit details, ansatz choices, and calibration parameters are provided in the next section.

These results provide an early but concrete demonstration of how quantum components may be meaningfully integrated into classical PDE solvers, offering scalable hybrid strategies even within the noise and qubit limitations of current quantum hardware.

#### Appendix B: Implementation of QIML on the emulator and IQM Devices

In the QIML framework proposed in this work, the quantum component is realized using a parameterized quantum circuit as a quantum generator. Its core function, learning invariant distributions from observational data, has been outlined in the preceding section. Here, we detail the implementation of this quantum model on the classical emulator and superconducting quantum hardware provided by IQM [69]. A classical emulator is a conventional computer program that simulates the mathematical operations of an ideal, noise-free quantum device. Due to experimental resource constraints, real quantum hardware implementation was conducted only on the most challenging benchmark—the turbulent channel flow dataset.

## 1. Quantum Circuit Architecture and Parameterization

We construct our quantum circuit using a layered structure composed of parameterized single-qubit rotations followed by entangling operations. The circuit uses Qiskit and consists of L=3 to 8 alternating layers. Each layer comprises three rotation gates per qubit:  $R_y(\theta_i)$ ,  $R_z(\phi_i)$ , and  $R_x(\psi_i)$  which are all transpiled to local rotation gate, followed by a sequence of controlled-Z (CZ) gates between adjacent qubits. The number of qubits n ranges from 10 to 15, depending on the resolution of the discretised target distribution.

$$U(\boldsymbol{\theta}) = \prod_{\ell=1}^{L} \left[ \left( \prod_{j=1}^{n} R_{x}^{(j)} (\psi_{j}^{(\ell)}) R_{z}^{(j)} (\phi_{j}^{(\ell)}) R_{y}^{(j)} (\theta_{j}^{(\ell)}) \right) \left( \prod_{(j,k) \in \mathcal{C}} CZ_{j,k} \right) \right],$$
(B1)

The full quantum state  $|\psi_{\theta}\rangle = U(\theta)|0\cdots 0\rangle$  is sampled N times to generate empirical frequencies  $\hat{p}_{\theta}(x)$  used to approximate the target distribution.

Notably, we do not inject explicit classical features into the quantum circuit. Instead, the quantum module acts purely as a generative module: its parameters are optimized so that the Born distribution reproduces the empirical statistics of the data. This choice eliminates costly quantum-to-classical data interfacing and highlights the expressive power of comparatively shallow circuits for modeling complex, high-dimensional distributions.

A parameterized quantum state  $|\psi_{\theta}\rangle$  lives in a  $2^n$ -dimensional Hilbert space, where the amplitudes  $\langle x|\psi_{\theta}\rangle$  define a probability distribution over computational basis states. Each basis string x is mapped bijectively to a spatial grid point, so the quantum state provides an implicit embedding of the target measure into a linear feature space. Unlike explicit kernel expansions, however, this Hilbert-space representation is generated by a quantum circuit whose entangling gates can capture non-local correlations—potentially including quantum entanglement—without the need for an exponential number of classical parameters.

This construction allows for efficient sampling and generalization from complex distributions. Classical networks often require thousands of parameters to represent distributions with long-range correlations or multi-modal structure. In contrast, our Q-Prior uses fewer parameters and leverages the quantum state's exponential support to encode richer structure in the generated samples. This trade-off between circuit expressivity and parameter efficiency is particularly valuable under the constraints of quantum hardware.

## 2. Implementation of QIML

We implemented and validated the classical machine learning and quantum emulator on BEAST GPU cluster from Leibniz Supercomputing Centre and the quantum generator on superconducting quantum hardware provided by IQM, mainly using the 20-qubit *Garnet* chip. A subset of 10 qubits was selected based on individual coherence performance and gate error metrics. The above circuit is compiled to superconducting hardware using IQM's transpiler stack. Transpilation includes single- and two-qubit gate fusion, qubit remapping, and hardware-specific gate decompositions. A representative transpiled circuit for the 10-qubit Garnet chip is shown in Appendix Fig. 8, illustrating the translation

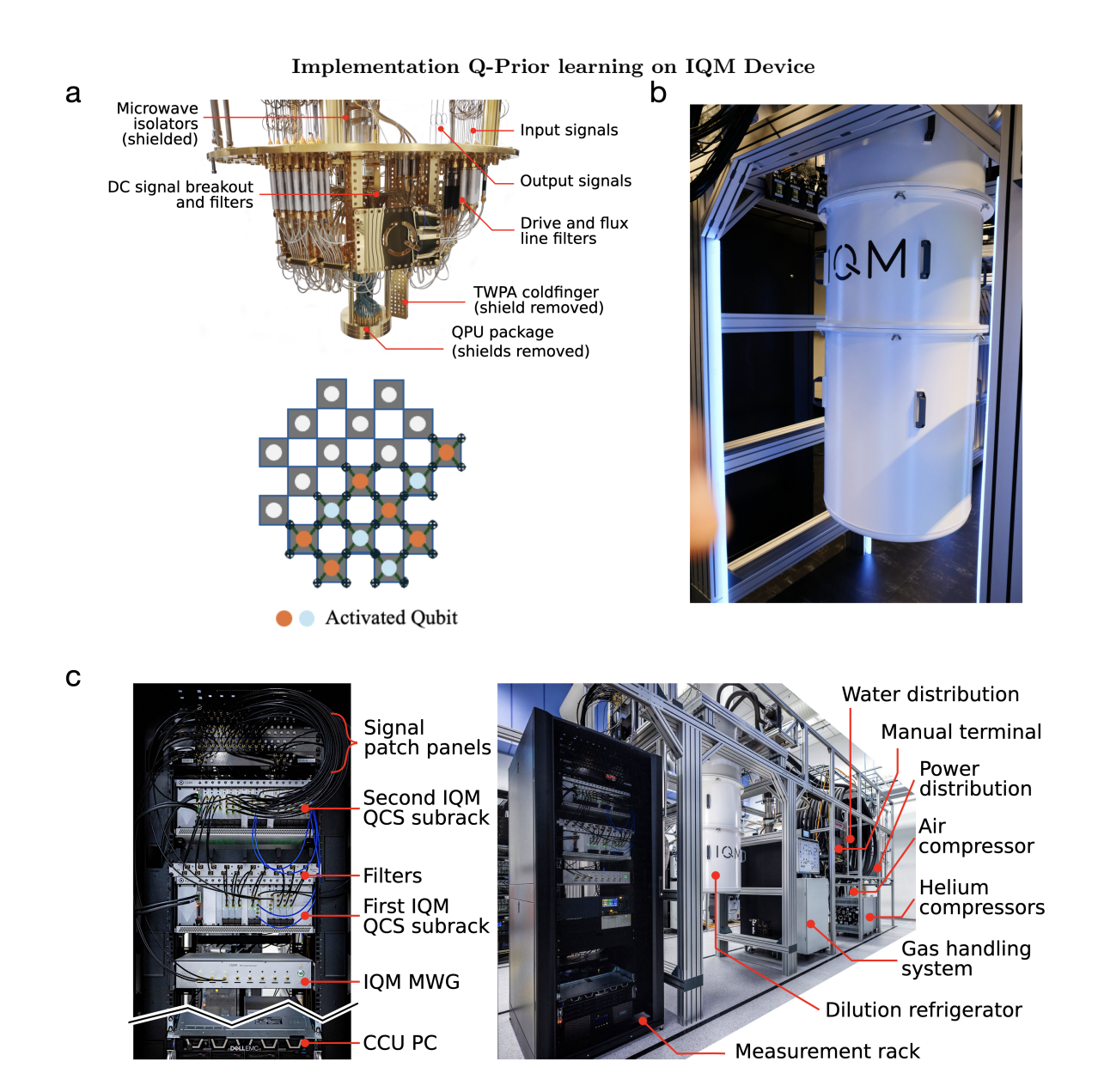


FIG. 8. Representative images of the IQM Radiance 20 quantum computer (Garnet). Copyright permission from IQM. a. Cryogenic components inside the host dilution refrigerator. 10 qubits are used of the 20-qubit IQM computer. b. IQM's quantum computer is housed within an ultra-high vacuum cryostat during operation, maintaining the ultra-low temperatures required for superconducting qubit performance. c. Photograph of the IQM system without covers.

of  $R_y/R_z/R_x$  blocks into native  $R(\theta,\phi)$  rotations with optimized layout and connectivity. The total number of parameters is approximately bounded by 300, as each qubit hosts 2–3 rotation gates per layer (each with a trainable parameter), and the circuit involves up to 10 qubits and 10 layers.

Each quantum circuit is executed with  $N=20{,}000$  measurement shots on the emulator and quantum devices, yielding samples  $\{x_i\}_{i=1}^N$  distributed according to the Born rule, i.e., with probabilities  $|\langle x_i|\psi_\theta\rangle|^2$ . These are post-processed into traditional histograms and compared to the empirical fluid velocity distribution via KL divergence, MMD loss, and peak structure preservation losses. Sampling outcomes typically yield  $8000-20{,}000$  distinct outcomes per shot batch, corresponding to 10-15-bit strings depending on circuit size. All remaining traditional computation, including forward simulation and loss evaluation, was executed on NVIDIA A100 GPUs.

## Quantum Circuit Architecture and Error mitigation

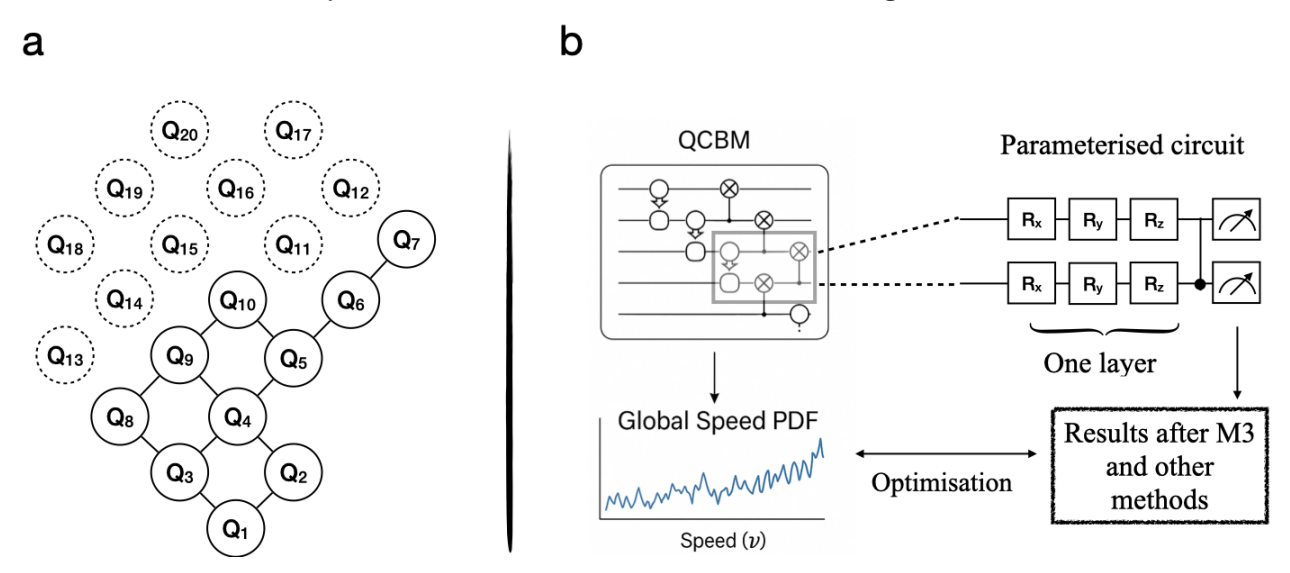


FIG. 9. a. We use 10 high-fidelity qubits of the 20 qubits available on IQM-Garnet. b. Diagram of the quantum circuit architecture and error mitigation methods.

## 3. Optimization Strategy and Training Protocol

The training for the Kuramoto-Sivashinsky and Kolmogorov flow systems was conducted on a quantum circuit emulator, which is a classical simulation of an ideal quantum device supported by the PennyLane and Qiskit libraries, optimized by Adam. Given its higher complexity and the failure of classical models to learn its dynamics, the TCF system was used for validation on real quantum hardware, accessed via Qiskit and the IQM-Qiskit provider. As shown in Fig. 10, for the training on the hardware, our optimization of quantum generator parameters was carried out using several traditional algorithms, with L-BFGS yielding the most stable convergence under hardware noise. Across all simulations and experiments, and depending on dataset complexity and resolution, training epochs varied between 400 and 500. The number of learnable parameters, corresponding to the angles of the parameterized rotation gates within the quantum circuit as shown in Fig. 9, ranged from 120 to 300. For the specific parameter count for each system, we refer the reader to table III and table IV in our discussion on parameter efficiency and memory advantage. Target distributions were generated by binning velocity fields from turbulent and Kolmogorov flow datasets into one-dimensional histograms with support ranging from  $2^{10} = 1024$  to  $2^{15} = 32,768$  bins.

#### 4. Sensitivity of Hardware Quantum Generator to Qubit Number and Circuit Depth

To better understand the scalability limitations of Q-priors on real quantum hardware, we conducted an ablation study by varying both the number of active qubits (from 4 to 15) and the circuit depth (from 2 to 12 layers) on the IQM superconducting processors. As shown on the IQM official website, increasing either the qubit count or the number of layers leads to a marked rise in total circuit error, which in turn degrades the quality of the sampled distributions—particularly their ability to reproduce accurate velocity statistics.

This degradation is primarily due to the accumulation of readout noise and gate errors, which increase non-linearly with circuit size. In contrast to noiseless simulators or emulators, real hardware suffers from decoherence, sampling noise, and hardware-specific imperfections that compound as more gates and qubits are used. These effects place practical constraints on how expressive a quantum circuit can be without error correction. Such challenges are hallmarks of the present NISQ era, where the accumulation of errors fundamentally limits computational power.

To address these limitations, we apply hardware-aware strategies including targeted chip and qubit selection, suitable circuit depth, and error mitigation, which are detailed in the following section.

#### quantum generator results obtained using different optimization methods

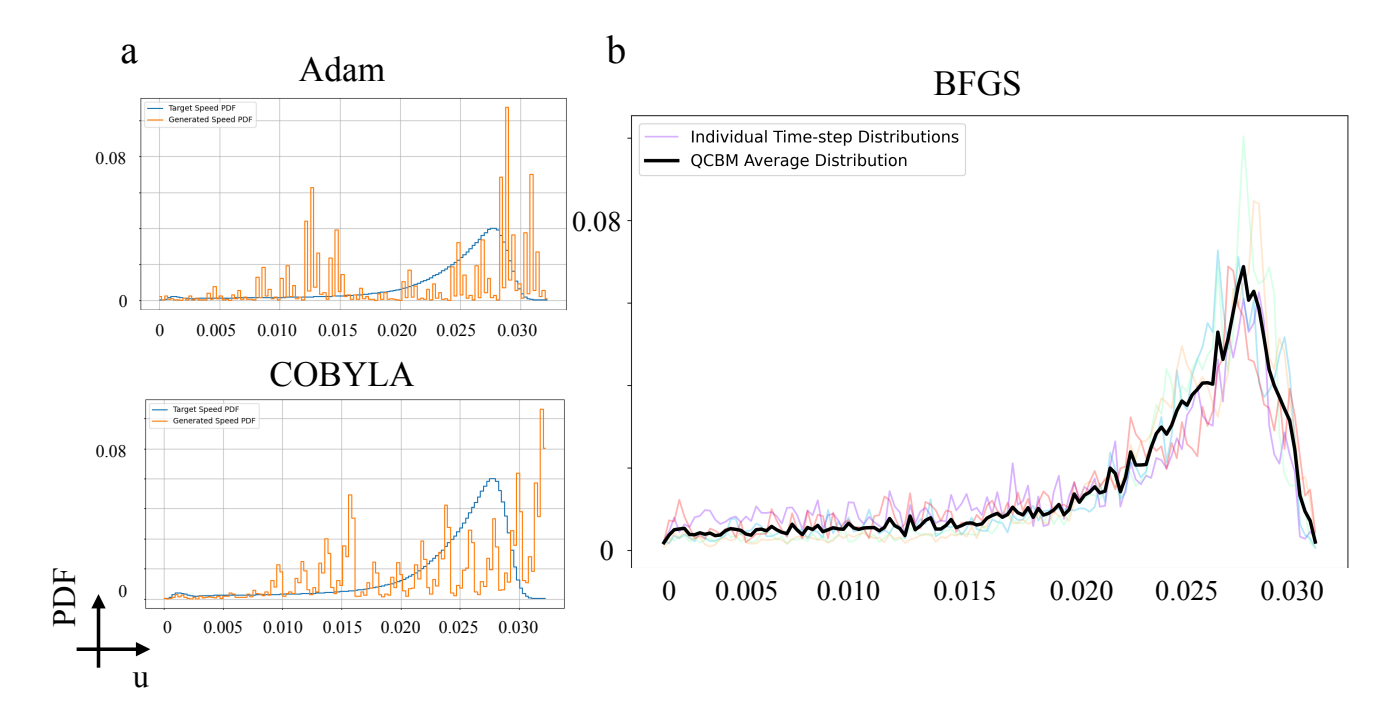


FIG. 10. a. Training with Adam and COBYLA optimizers results in poor convergence and noisy distributions. b. Applying a single-shot L-BFGS optimizer in combination with the M3 measurement mitigation technique yields significantly improved performance.

## 5. Chip Selection, Error Mitigation and Robustness Analysis

As shown in IQM official website and Fig. 11, our initial experiments using IQM's Sirius chip yielded not good convergence due to fidelity limitations, two-bit gate connection limitations due to hardware topology, and the inherent sensitivity of high-resolution distributions to noise. The technical specifications and performance metrics, including coherence times and gate fidelities, for the Sirius and Garnet quantum processors are summarized in Table II. To mitigate these issues, we first migrated our algorithm to the Garnet high-fidelity architecture and reduced histogram binning granularity from 1024 to 256. To mitigate the effect of readout errors during quantum sampling, we implemented a post-processing strategy based on the matrix-free measurement mitigation (M3) protocol [70] shown in Fig. 9. This technique calibrates the readout noise by learning a probabilistic response model from the device's native measurement behavior. Then it applies Bayesian corrections to raw bitstring outputs without explicitly inverting a response matrix, thereby preserving numerical stability at scale. The use of M3 proved particularly valuable given the multi-qubit readout complexity and the high measurement resolution required to fit fine-grained distributional features.

In addition to M3, we employed a combination of large-sample averaging and outlier rejection to suppress noise further. One key feature of our framework is the one-time, offline training of the Q-prior. The quantum generator is trained for a total of 50 epochs. Once this initial training process is complete, the quantum circuit is no longer needed for the main training loop. Within each of the 50 training epochs, each quantum circuit was executed with up to 20,000 shots, and the resulting histograms were averaged across repeated trials to stabilize statistical fluctuations. Outlier detection routines were applied to eliminate anomalous measurement rounds—specifically, instances where a disproportionate number of outcomes collapsed into trivial all-zero or all-one configurations. These spurious distributions, often symptomatic of transient decoherence or control drift, were discarded from the final ensemble to avoid biasing the learned quantum distribution. Together, these techniques enabled robust extraction of high-dimensional statistical structure from quantum circuits on quantum hardware. Circuit transpilation was performed via IQM's native compiler stack, which supports qubit mapping, single-gate merging, and readout-aware optimization. These improvements allowed us to stabilize the training loss and achieve consistent sampling performance across multiple

TABLE II. Comparison of Quantum Processor Specifications for Sirius and Garnet.

Property	Sirius	Garnet
Topology	STAR 24	CRYSTAL 20
Qubits	16	20
Pulse-Level Access	Available	Not available
Native Gates	barrier, cz, measure, move,	prx barrier, cz, measure, prx
Max Circuits / Shots	500 / 20000	500 / 20000
Median T1	$29.33 \ \mu s$	$38.96~\mu \mathrm{s}$
Median T2 (Ramsey)	$23.30 \ \mu s$	$7.78~\mu\mathrm{s}$
Median T2 (Echo)	$30.20 \ \mu s$	$16.95 \ \mu s$
Median PRX Gate Fidelity	99.89 %	99.89~%
Median CZ Gate Fidelity	98.27 %	99.29~%
Median Move-Move Fidelity	98.96~%	Not listed

Quantum Generator results obtained on different IQM quantum devices

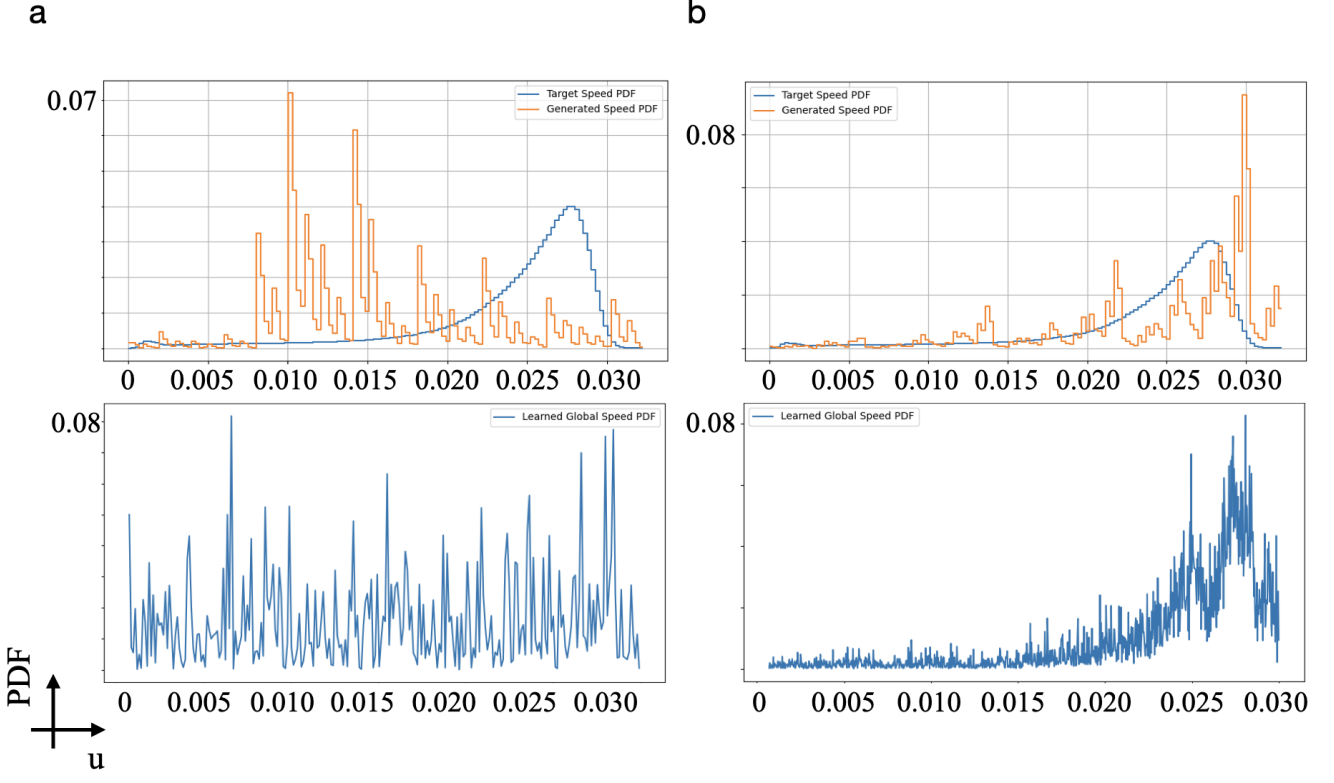


FIG. 11. a. Training on IQM-Sirius results in poorer distributions. b. Quantum Generator achieves better results on IQM-Garnet.

runs. We tested numerous qubit configurations on both 10-qubit and 15-qubit hardware layouts. Results show that expressive distributions can be reliably approximated using  $\sim$ 120 parameters, with deeper circuits providing better capture of multimodal or heavy-tailed distributions. The absence of input encoding enables this model to generalize across different datasets (e.g., Kolmogorov flow and shear-driven turbulence) by retraining only on the output distribution. We observed consistent convergence behaviors across independent runs, with less than 5% variance in MMD divergence across 5 seeds.

Furthermore, we found that higher-resolution distributions exhibit increased robustness against circuit-level noise, while low-resolution cases suffer from distributional collapse and mode imbalance. The experimental evidence suggests that quantum circuits are particularly well-suited to modeling high-dimensional dynamical systems. These findings support the feasibility of embedding small-scale quantum devices within traditional learning pipelines. The successful deployment of quantum generators on real quantum hardware, together with GPU-based optimization and software differentiation, illustrates a viable hybrid computing paradigm for physics-informed machine learning.

## Appendix C: Kuramoto-Sivashinsky Equation

The Kuramoto-Sivashinsky (KS) equation is a fourth-order nonlinear partial differential equation that models spatiotemporal instabilities in a range of physical systems [101, 102]. It is especially important in the study of pattern formation and chaos. The governing equation is described as follows.

## 1. Governing Equation

In one spatial dimension, the KS equation is written as:

$$\frac{\partial u}{\partial t} + u \frac{\partial u}{\partial x} + \frac{\partial^2 u}{\partial x^2} + \nu \frac{\partial^4 u}{\partial x^4} = 0, \tag{C1}$$

where u(x,t) is a scalar field, x is the spatial coordinate, t is time, and  $\nu$  is a positive parameter controlling the strength of the fourth-order dissipation term. The term  $\frac{\partial u}{\partial t}$  describes the temporal evolution of the field. The nonlinear term  $u\frac{\partial u}{\partial x}$  represents convective transport and introduces nonlinearity into the system. The second derivative term  $\frac{\partial^2 u}{\partial x^2}$  acts as a linear destabilizing mechanism, similar to anti-diffusion, amplifying short-wavelength perturbations. The fourth derivative term  $\nu \frac{\partial^4 u}{\partial x^4}$  provides a stabilizing effect by damping high-frequency modes, thereby preventing blow-up and enabling bounded chaotic behavior.

#### 2. Boundary Conditions

In this study, the KS equation is performed under periodic boundary conditions of the form: u(x + L, t) = u(x, t), where L is the spatial period of the domain. These conditions reflect the translational symmetry of many physical systems and simplify the analysis of chaotic dynamics.

#### 3. Data Source

In the first application, we performed KS equation dataset with the help of CFD jax community code [103]. The dataset has also been used and validated in Ref. [35].

## Appendix D: Kolmogorov Flow Governing Equation

The Kolmogorov flow is governed by the incompressible Navier-Stokes (NS) equations with a sinusoidal forcing term. In this paper, we apply a 2D Kolmogorov flow as an example to examine our QIML framework. Below, we will describe our system in 2D NS equations with forcing.

## 1. Navier-Stokes Equations with Forcing

The flow is described by the incompressible Navier-Stokes equations with an external forcing term, which is denoted as

$$\frac{\partial \mathbf{u}}{\partial t} + (\mathbf{u} \cdot \nabla)\mathbf{u} = -\nabla p + \nu \nabla^2 \mathbf{u} + \mathbf{F},\tag{D1}$$

$$\nabla \cdot \mathbf{u} = 0, \tag{D2}$$

where  $\mathbf{u} = (u(x, y, t), v(x, y, t))$  is the velocity vector field of the fluid, p(x, y, t) is the scalar pressure field,  $\nu$  is the kinematic viscosity, and  $\mathbf{F}$  represents the external body force applied to the fluid.

#### 2. Kolmogorov Forcing

In the Kolmogorov setup, the force is applied only in the x-direction and varies sinusoidally in the y-direction. The forcing term is defined as:

$$\mathbf{F} = (F_0 \sin(ky), 0), \tag{D3}$$

where  $F_0$  is the amplitude of the forcing and k is the wavenumber determining the periodicity in the y-direction.

#### 3. Data Source

In the second application, we utilized the high-fidelity Kolmogorov dataset derived from [104], which offers a comprehensive and statistically rich representation of turbulent flow fields. This dataset was critical for evaluating the robustness and generalization of our proposed model, particularly under complex conditions characterized by a high Reynolds number of Re = 1000. It comprises 40 trajectories, each containing 320 temporal snapshots, with a spatial resolution of  $256 \times 256$  grid points. To establish a high-fidelity ground truth, all numerical simulations for data generation were performed using double-precision (FP64) floating-point arithmetic. For the machine learning stage, however, our QIML framework operates entirely in single-precision (FP32) during both training and inference, a standard practice to balance computational efficiency and numerical stability. Consequently, while the models are trained on FP64 data, their predictive outputs are themselves of FP32 precision. The extent to which training the QIML framework in double-precision would alter these predictive outcomes remains a subject for future study.

## Appendix E: LBM-based 3D turbulent channel flow simulation

#### 1. The Lattice Boltzmann Method

The Lattice Boltzmann Method is known as an alternative computational fluid dynamics (CFD) framework that models the evolution of single particle distribution functions at the kinetic-level. It is based on the discrete form of the Boltzmann equation and operates on a lattice grid in space and time. The governing equation for the probability distribution function, or populations  $\mathbf{f}$ , located at position  $\mathbf{x}$  at time t, accounting for both collisions and external forces, is given by:

$$\mathbf{f}(\mathbf{x} + \mathbf{c}_i \Delta t, t + \Delta t) = \mathbf{f}(\mathbf{x}, t) + \Omega \left( \mathbf{f}(\mathbf{x}, t) \right) + \mathbf{F}(\mathbf{x}, t), \tag{E1}$$

where  $\mathbf{c}_i$  are the discrete lattice velocities,  $\Delta t$  is the simulation time step which is set to unity,  $\Omega$  is the collision operator for the probability distribution function.  $\mathbf{F}$  is the external volume force.

The LBE has gained popularity due to its simplicity, ease of implementation on parallel architectures, and its ability to naturally handle complex boundary conditions. Macroscopic fluid quantities such as density and velocity are obtained by taking moments of the distribution function. Specifically, the fluid density  $\rho$  and momentum density  $\rho$ **u** are computed as follows:

$$\rho(\mathbf{x},t) = \sum_{i=0}^{Q-1} f_i(\mathbf{x},t), \tag{E2}$$

$$\rho(\mathbf{x}, t)\mathbf{u}(\mathbf{x}, t) = \sum_{i=0}^{Q-1} f_i(\mathbf{x}, t)\mathbf{c}_i,$$
(E3)

where  $f_i(\mathbf{x},t)$  is the particle distribution function in the *i*-th discrete velocity direction at position  $\mathbf{x}$  and time t.

## 2. Bhatnagar–Gross–Krook Collision Kernel

We define BGK collision kernel  $\Omega$  as follow:

$$\Omega\left(\mathbf{f}(\mathbf{x},t)\right) = -\frac{1}{\tau}(\mathbf{f}(\mathbf{x},t) - \mathbf{f}^{\text{eq}}(\mathbf{x},t)), \tag{E4}$$

where  $\mathbf{f}^{\text{eq}}(\mathbf{x},t)$  denoted as the equilibrium distribution function,  $\tau$  is correlated with the kinematic viscosity  $\nu$ :

$$\nu = c_s^2 \left(\tau - \frac{1}{2}\right) \Delta t_{coll},\tag{E5}$$

where  $\Delta t_{coll}$  is set to identity in the simulation.

#### 3. Smagorinsky Subgrid-Scale Modeling

In this part, we summarize the lattice-Boltzmann-based Smagorinsky Subgrid Scale (SGS) LES techniques. Within the LBM framework, the effective viscosity  $\nu_{\rm eff}$  [105–107] is modeled as the sum of the molecular viscosity,  $\nu_0$ , and the turbulent viscosity,  $\nu_t$ :

$$\nu_{\text{eff}} = \nu_0 + \nu_t, \qquad \nu_t = C_{\text{smag}} \Delta^2 |\bar{\mathbf{S}}|, \tag{E6}$$

where  $|\bar{\mathbf{S}}|$  is the filtered strain rate tensor,  $C_{\rm smag}$  is the Smagorinsky constant,  $\Delta$  represents the filter size, which is set to 1 LBU. The Smagorinsky constant for this study is set to  $C_{\rm smag} = 0.01$ .

#### 4. Simulation Set up

In this study, the computational domain for the turbulent channel flow simulation is defined with dimensions  $L_x \times L_y \times L_z = 1024 \times 192 \times 192$ , where x, y, and z denote the streamwise, vertical, and spanwise directions, respectively. The friction Reynolds number is set to  $Re_{\tau} = 180$  which is equivalent to Re = 3250. Periodic boundary conditions are applied in the streamwise and spanwise directions, while the vertical direction is governed by no-slip boundary conditions [108]. This configuration distinguishes our dataset from existing studies that primarily rely on 2D turbulent cases, as our dataset is based on fully three-dimensional simulations. The fully developed 3D turbulent channel flow simulation follows the configuration outlined in reference [77]. The simulation begins from an initial zero-velocity field, with a square block of size  $20 \times 20 \times 100$  grid points positioned at x = 192. A volumetric force is applied uniformly across the domain to drive the flow. The simulation is run for 50 domain-through times to establish initial flow characteristics. After this initial phase, the block is removed, and the simulation is continued for an additional 50 domain-through times, allowing the flow to fully develop into a turbulent state. Data sampling begins after this stage, focusing on the 2D cross-section at x = 512. Data is collected over a further 100 turnover times, ensuring that the samples represent fully developed turbulence. The simulation timestep is set to  $\Delta t = 0.02$  s, and it operates in dimensionless units (800 timesteps), as is typical for LBM simulations. The detailed transformation from dimensionless units to physical units can be found in section S6. To ensure robustness and generality, we conducted three independent 3D turbulent channel flow simulations under these conditions, generating a comprehensive dataset for analysis.

## 5. Dataset Periodic Turbulent Channel Flow Validation

Fig. 12 presents a comparison between the streamwise mean velocity profile obtained from our large eddy simulation using the lattice Boltzmann method (LES-LBM) and benchmark direct numerical simulation (DNS) data at a friction Reynolds number of Re $\tau$  = 180. The velocity is normalized in wall units, where  $u^+ = u/u_{\tau}$  and  $y^+ = yu_{\tau}/\nu$ . The LES-LBM result shows good agreement with the DNS reference across both the viscous sublayer and the logarithmic region, indicating that the model successfully captures key features of wall-bounded turbulence under periodic boundary conditions.

Fig. 13 shows the comparison of RMS velocity fluctuations between our LES–LBM simulations and DNS data at  $\text{Re}_{\tau}=180$ . The LES–LBM results (solid lines) exhibit good agreement with DNS (dashed lines), particularly in reproducing the characteristic peak in  $u_{\text{rms}}^{+'}$  near  $y^+\approx 15$  and capturing the general anisotropic distribution of turbulent fluctuations across the channel height.

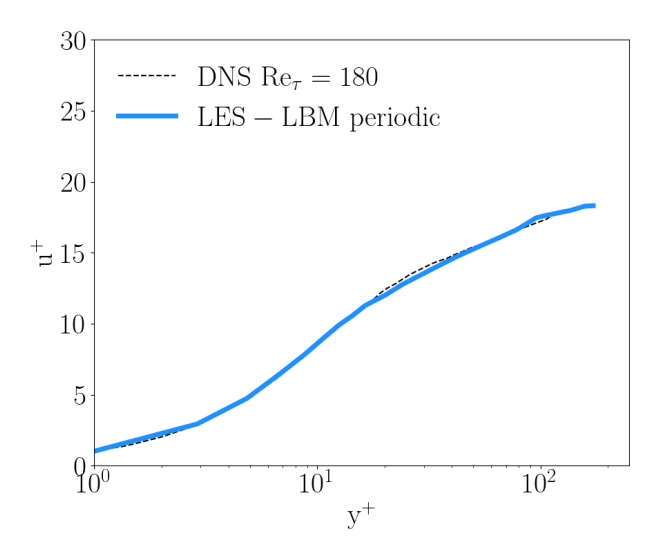


FIG. 12. Comparison of dimensionless mean streamwise velocity profiles in wall units ( $u^+$  vs.  $y^+$ ) between the LES–LBM simulation with periodic boundary conditions and DNS data at Re<sub> $\tau$ </sub> = 180. The LES–LBM result (solid blue) closely follows the reference DNS profile (dashed black), validating the accuracy of the LBM in capturing the near-wall behavior and log-layer scaling of turbulent channel flow.

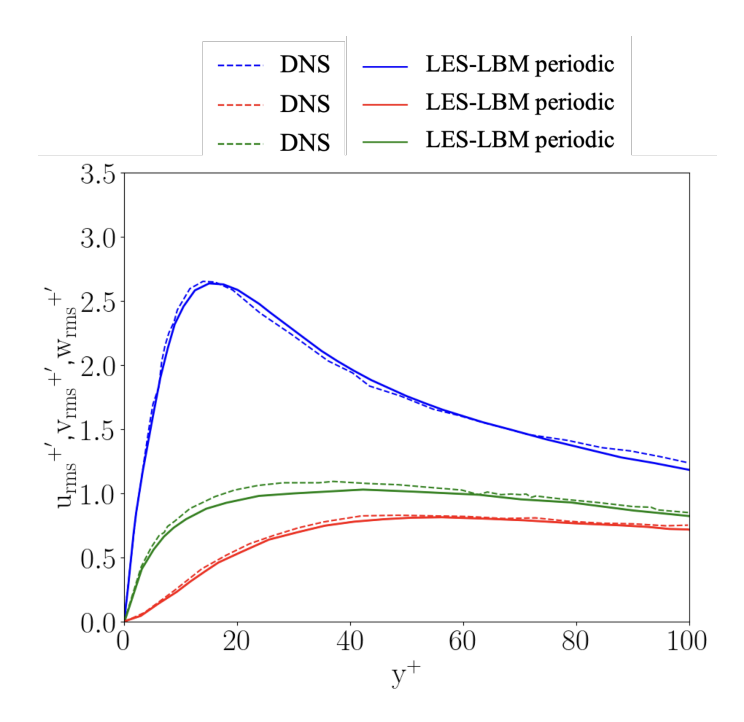


FIG. 13. Comparison of root-mean-square (RMS) velocity fluctuations in dimensionless wall units between LES-LBM simulations with periodic boundary conditions and DNS data at  $\text{Re}_{\tau}=180$ . The streamwise (blue), wall-normal (red), and spanwise (green) RMS components are shown. The LES-LBM results (solid lines) closely match the DNS reference (dashed lines), particularly in the near-wall region, capturing the peak in  $u_{\text{rms}}^{+\prime}$  and maintaining the correct anisotropy among components.

## 6. The Multiple-Relaxation Time Lattice Boltzmann Moment Space Transformation Matrix

Let's revisit the evolution equation for the distribution functions expressed as:

$$\mathbf{f}(\mathbf{x} + \mathbf{c}_i \Delta t, t + \Delta t) = \mathbf{f}(\mathbf{x}, t) - \mathbf{M}^{-1} \mathbf{S} \mathbf{M} \left[ \mathbf{f}(\mathbf{x}, t) - \mathbf{f}^{\text{eq}}(\mathbf{x}, t) \right] + \mathbf{F}(\mathbf{x}, t) \Delta t, \tag{E7}$$

where  $\mathbf{M}$  denotes the moment space transformation matrix for the multiple relaxation time (MRT) collision kernel[109]. The matrix M can be defined as:

Appendix F: Unit Conversion between LBM Units and Physical Units

In this subsection, we demonstrate the unit conversion between LBU and physical units in both velocity and distance. Within the LBM simulation, we can obtain the LBM velocity  $\mathbf{u}_{LB}(\mathbf{x},t)$  at location  $\mathbf{x}$ . The physical unit of the velocity,  $\mathbf{u}_{phys}(\mathbf{x},t)$ , can be written as

$$u_{\text{phys}}(\mathbf{x}, t) = u_{\text{LB}}(\mathbf{x}, t) \frac{c_x}{c_t},$$
 (F1)

where  $c_x$  and  $c_t$  are the conversion factors from the lattice Boltzmann simulation to the physical system, which is defined as

$$c_x = \frac{L_{\text{phys}}}{L_{\text{LB}}}, \qquad c_t = \frac{t_{\text{phys}}}{t_{\text{LB}}},$$
 (F2)

where  $L_{\text{phys}}$  and  $t_{\text{phys}}$  represent the space and time units from the physical system, while  $L_{\text{LB}}$  and  $t_{\text{LB}}$  are the space and time lattice Boltzmann units from the lattice Boltzmann simulation. Accordingly, we can also obtained the physical distance  $y_{\text{phys}}$  from the LBM length scale:

$$y_{\rm phys} = y_{\rm LB}c_x. \tag{F3}$$

For example, in Eq. F2,  $L_{\rm phys}$  may denote the height of the channel as  $L_{\rm phys}=2{\rm m}$  so that  $L_{\rm LB}=20$  LBU. Then,  $c_x=0.1{\rm m}$ . Similar calculations can be performed to determine the time scale conversion factor  $c_t$ .

## Appendix G: Neural Networks Architecture Details

#### 1. Quantum Machine Learning Model Architecture

The quantum machine learning model consists of parameterized quantum circuits trained to approximate target Q-Priors via a quantum generator; the optimization is performed traditionally through gradient-based updates, as detailed in Appendix A and illustrated in Fig.1 of the main text.

In our hybrid architecture, quantum and traditional computations are optimized independently but operate in a tightly coupled feedback loop. The outputs of traditional modules dynamically guide quantum circuit objectives, establishing a synergistic interaction that underscores the relevance and practicality of hybrid quantum—traditional integration.

#### 2. Model Architecture for 2D chaotic flows

The Koopman-based model begins with a patch embedding layer implemented using a single 2D convolutional layer. This layer transforms the input from 1 channel to 32 channels while maintaining a spatial resolution of (64, 64). No activation function is specified for this layer.

Following the embedding, the encoder consists of three transformer blocks. The first block contains 2 layers and maps features from 32 channels to 64 channels, reducing the spatial dimensions to (32,32), with ReLU activations. The second block has 3 layers and increases the channels from 64 to 128 while downsampling to (8,8), again using ReLU activations. The third block also comprises 3 layers, maintaining 128 channels and compressing the spatial dimensions to (2,2), with ReLU activation applied.

After encoding, the representation is passed through a fully connected layer that operates on a flattened feature vector of size  $128 \times 2 \times 2$ . The activation function is not specified for this operator. Next, the model includes a fully connected layer applied to the same flattened  $128 \times 2 \times 2$  feature vector, without a specified activation.

A third component, the backward component, is similarly implemented using a fully connected layer acting on the  $128 \times 2 \times 2$  vector, with no activation mentioned.

The decoder mirrors the encoder architecture in reverse. The first decoder block uses 3 transformer layers to maintain 128 channels and upsample to (8,8) with ReLU activation. The second block also has 3 layers, reducing the channels from 128 to 64 and increasing the spatial resolution to (32,32), again with ReLU. The third block consists of 2 layers, mapping 64 channels to 32 with output size (64,64) and ReLU activations. Finally, a single 2D convolutional layer reduces the channels from 32 back to 1 while preserving the (64,64) spatial resolution, with no activation specified.

Parameter comparison across different models (QIML, Koopman, FNO and MNO) can be found in Table III.

#### 3. Fourier Neural Operator Architecture

The Fourier Neural Operator is a neural network architecture designed to learn mappings between function spaces, with a particular focus on solving partial differential equations and modeling spatial-temporal systems. Unlike traditional convolutional networks, it operates in the frequency domain, enabling efficient learning of long-range dependencies.

The processing pipeline in this paper consists of three main stages:

**Lifting**, which maps the input tensor from  $C_{\rm in} = 1$  to  $C_{\rm hidden} = 128$  channels using a  $1 \times 1$  convolution:

$$\mathbf{X}_1 = \operatorname{Conv}_{1 \times 1}(\mathbf{X}_0), \tag{G1}$$

where  $\mathbf{X}_0 \in \mathbb{R}^{B,1,H,W}$  and  $\mathbf{X}_1 \in \mathbb{R}^{B,128,H,W}$ .

Four Fourier layers, each of which is formed by spectral convolutional blocks with residual connections. The spectral convolution block first applies a 2D Fast Fourier Transform to the input tensor along its spatial dimensions. Then, a mode truncation step retains only the lowest  $n_{\text{mode}} = (32, 32)$  frequency components. These retained modes are acted upon by complex-valued spectral weights  $\mathbf{W}_{\text{spec}} \in \mathbb{C}^{C_{\text{out}} \times C_{\text{in}} \times 32 \times 32}$ . To reduce storage and computational cost, these spectral weights are factorized using Tucker factorization as:

$$\mathbf{W}_{\text{spec}} \approx \mathbf{U}_{\text{out}} \times \mathbf{G} \times \mathbf{U}_{\text{in}},$$
 (G2)

where  $\mathbf{U}_{\mathrm{in}} \in \mathbb{R}^{C_{\mathrm{in}} \times r_{\mathrm{in}}}$ ,  $\mathbf{U}_{\mathrm{out}} \in \mathbb{R}^{C_{\mathrm{out}} \times r_{\mathrm{out}}}$  and  $\mathbf{G} \in \mathbb{C}^{r_{\mathrm{in}} \times r_{\mathrm{out}} \times 32 \times 32}$ . The modified spectrum is then transformed back to the spatial domain via an inverse FFT. In parallel, a pointwise convolution path applies a  $1 \times 1$  convolution to the original input tensor to retain local information. Finally, a residual connection combines these paths with the original input, followed by a GELU non-linear activation function:

$$\mathbf{X}_{\mathcal{L}+1} = \sigma(\operatorname{Spectral}(\mathbf{X}_{\mathcal{L}}) + \operatorname{Pointwise}(\mathbf{X}_{\mathcal{L}}) + \mathbf{X}_{\mathcal{L}}). \tag{G3}$$

**Projection**, the final stage, which reduces the hidden representation from  $C_{\text{hidden}} = 128$  to  $C_{\text{out}} = 1$  channels using a 2-layer  $1 \times 1$  convolutional MLP:

$$\mathbf{Y} = \operatorname{Conv}_{1 \times 1}(\sigma(\operatorname{Conv}_{1 \times 1}(\mathbf{X}_{\mathcal{L}}))), \tag{G4}$$

with intermediate channels set to  $r_{\text{proj}} \times C_{\text{hidden}} = 1 \times 128 = 128$ .

See Table III for the total parameters of the FNO model.

## 4. Markov Neural Operator Architecture

The Markov Neural Operator is a framework to learn discretization-independent mappings between function spaces. In this approach, the learned operator is expressed as a finite composition of Markov kernel layers, each representing a local operator that evolves the state over a discrete step in "operator depth."

The architecture setting in this paper consists of three main stages:

**Lifting**, where a  $1 \times 1$  convolution projects the input tensor from  $C_{\rm in} = 1$  to  $C_{\rm hidden} = 128$ :

$$\mathbf{X}_1 = \operatorname{Conv}_{1 \times 1}(\mathbf{X}_0), \tag{G5}$$

where  $\mathbf{X}_0 \in \mathbb{R}^{B,1,H,W}$  and  $\mathbf{X}_1 \in \mathbb{R}^{B,128,H,W}$ .

Single Markov kernel block, which consists of four sequential Markov kernel layers. Each layer is implemented via a spectral convolution in Fourier space combined with local pointwise updates, following a similar setting as the FNO architecture described previously. A residual connection combines these paths, but the non-linear activation function used is SELU. This composition ensures that each layer satisfies the Markov property, where the updated state depends only on the previous state.

**Projection**, the final stage, which reduces the hidden representation from  $C_{\rm hidden} = 128$  back to  $C_{\rm out} = 1$  channels. Another key part of the MNO is its explicit stability features, which are realized by incorporating dissipative target mappings and partition of unity post-processing in the training loop. First, training inputs are drawn using spherical shell sampling:

$$\mathbf{x} \sim \mathcal{U}(\mathcal{S}(R_{\text{inner}}, R_{\text{outer}}))$$
 (G6)

where  $S(r_1, r_2) = \{ \mathbf{v} \in \mathbb{R}^n | r_1 \le ||\mathbf{v}||_2 \le r_2 \}$ . This ensures diverse energy levels are present in the training set. Second, a baseline dissipative target mapping is defined as:

$$\mathcal{D}(\mathbf{x}) = s \cdot \mathbf{x} \,, \quad 0 < s < 1 \tag{G7}$$

where we use s = 0.8. This map serves as a stable fallback for states outside the data manifold. Finally, a partition of unity correction blends the learned mapping  $f_{\theta}$  with the dissipative baseline  $\mathcal{D}$  using a smooth partition of unity function  $\rho$ :

$$\hat{\mathbf{y}}(\mathbf{x}) = \rho(\|\mathbf{x}\|) \cdot f_{\theta}(\mathbf{x}) + (1 - \rho(\|\mathbf{x}\|)) \cdot \mathcal{D}(\mathbf{x})$$
(G8)

with  $\rho$  defined as a sigmoid function  $\rho = (1 + e^{s(r-c)})^{-1}$ , where c is the shift and s controls the transition steepness. This ensures a high-fidelity learned output when  $\rho \approx 1$  (inside the training region) and a stable dissipative fallback when  $\rho \approx 0$  (outside the training region).

See Table III for the total parameters of the MNO model.

TABLE III. Total parameter counts for the compared models.

Model	Total Parameters
Q-Prior (in the QIML)	≈300
QIML (this work)	4,535,172
Koopman	4,534,872
FNO	35,971,333
MNO	45,823,681

## 5. Integration of the Traditional Model and the Quantum Prior Guidance

In our hybrid framework, the integration of quantum and traditional components is achieved by embedding a quantum-learned invariant distribution into the loss function of a traditional machine learning model tasked with forecasting high-dimensional dynamical systems. This coupling is designed to address a fundamental limitation in traditional neural PDE solvers: while they can capture short-term evolution, their predictive accuracy typically deteriorates over longer horizons due to the accumulation of numerical error and sensitivity to initial conditions.

The traditional machine learning model, constructed using convolutional or transformer-based architectures, is trained to predict the next-step velocity field  $\hat{u}_{t+1}$  from a history of past states  $\{u_t, u_{t-1}, \dots\}$ . To enhance robustness in long-term rollouts, we incorporate a distributional Q-Prior  $p_{\theta}(x)$  learned by the quantum generator, which approximates the system's invariant measure.

The initial loss formulation includes a reconstruction term and a Kullback–Leibler divergence between the predicted and quantum-learned distributions:

$$\mathcal{L}_{total} = \mathcal{L}_{recon} + \mathcal{L}_{unitary} + \lambda_{KL} \mathcal{L}_{KL}, \tag{G9}$$

where

$$\mathcal{L}_{\text{unitary}} = |K^{\top}K - I|_F^2$$
, for details, see the main text, (G10)

$$\mathcal{L}_{\text{recon}} = |\hat{u}_{t+1} - u_{t+1}|^2, \tag{G11}$$

and

$$\mathcal{L}_{KL} = D_{KL} \left( \hat{q}(x) | p_{\theta}(x) \right), \tag{G12}$$

with  $\hat{q}(x)$  denoting the empirical distribution derived from the predicted field  $\hat{u}_{t+1}$ .

While this formulation successfully captures the global distributional shape, it often converges to a low-variance mean-field solution, insufficient to preserve local or high-frequency structures critical for short-term dynamics. To mitigate this, we introduce two additional constraints.

First, we add a MMD term to better match higher-order statistics:

$$\mathcal{L}_{\text{MMD}} = \left| \mathbb{E}x \sim \hat{q}(x) [\phi(x)] - \mathbb{E}x \sim p_{\theta}(x) [\phi(x)] \right|_{\mathcal{H}}^{2}, \tag{G13}$$

where  $\phi(x)$  is a feature mapping into a reproducing kernel Hilbert space.

Second, in some cases (TCF), we also incorporate a peak loss to explicitly align dominant modes of the predicted and target distributions:

$$\mathcal{L}_{\text{peak}} = |\text{TopK}(\hat{q}(x)) - \text{TopK}(p_{\theta}(x))|^{2},$$
(G14)

where TopK selects the highest-probability bins from both histograms.

The final training loss is a weighted combination of all four components:

$$\mathcal{L}_{\text{total}} = \mathcal{L}_{\text{recon}} + \lambda_{\text{KL}} \mathcal{L}_{\text{KL}} + \lambda_{\text{MMD}} \mathcal{L}_{\text{MMD}} + \lambda_{\text{peak}} \mathcal{L}_{\text{peak}}. \tag{G15}$$

This composite objective ensures that predictions remain consistent with the invariant statistics of the underlying physical system, while also preserving critical local features necessary for short- and mid-term forecasting. Our results demonstrate that Q-Priors can significantly enhance the stability and accuracy of machine learning models in high-dimensional chaotic regimes.

Fig. 14 presents the spatial distribution of the normalized velocity error across the domain under three modeling regimes. The top panel displays error patterns obtained without Q-Priors, revealing widespread, spatially incoherent deviations with peak errors exceeding 10%. Incorporating a Q-Prior from a classical emulator (middle panel) leads to a pronounced reduction in error magnitude and spatial variance, with the majority of regions falling below 4%. Further improvement is observed when employing the Q-Prior trained on real quantum hardware (bottom panel), where error distributions are both quantitatively reduced and exhibit greater spatial smoothness, indicating enhanced generalization and stability in chaotic regime reconstruction. Fig. 15 shows the TCF velocity magnitude distribution  $\hat{q}(x)$  predicted under the same three learning regimes (no Q-Prior, emulator-based Q-Prior, and hardware-based Q-Prior), compared to the empirical target distribution. Without quantum guidance, the model fails to capture the dominant statistical mode—both the modal peak and its amplitude are significantly misaligned. With simulator-based Q-Prior, the predicted distribution nearly perfectly matches the raw data in both location and shape, confirming the Q-Prior's capacity to encode high-dimensional invariant measures with minimal parameterization. Hardware-based Q-Prior introduces moderate deviations, including a downward shift in peak probability and a small modal displacement; however, the distribution remains substantially closer to the ground truth than the classical result.

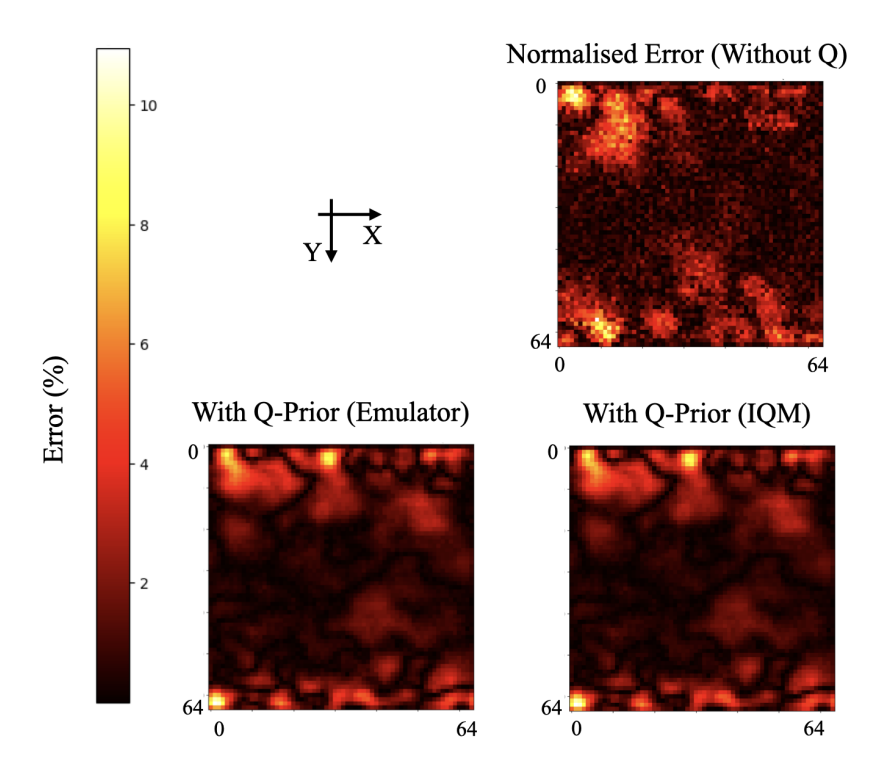


FIG. 14. Diagram of the normalized error of the turbulent channel flow. The baseline model without the Q-Prior (top right) is compared against the QIML model on a classical emulator (bottom left) and on IQM quantum hardware (bottom right). The QIML model demonstrates a marked reduction in error compared to its classical counterparts.

System	Qubits	Trainable $\theta$ parameters	Raw data (full set)	<b>Q-Prior file</b> (full set)	$\begin{array}{c} \mathbf{Compression} \\ \mathrm{(ratio)} \end{array}$	Device
Kuramoto-Sivashinsky	10	$\sim 120$	300 MB	$0.25~\mathrm{MB}$	$\approx 1.2 \times 10^3 : 1$	Emulator
2D Kolmogorov flow	10	$\sim 180$	$400~\mathrm{MB}$	$0.40~\mathrm{MB}$	$\approx 10^3 : 1$	Emulator
Turbulent channel flow	15	$\sim 300$	500  MB	2.3  MB	$\approx 2.2 \times 10^2 : 1$	Emulator
Turbulent channel flow	10	$\sim 240$	500  MB	$2.0~\mathrm{MB}$	$\approx 2.5 \times 10^2 : 1$	${\rm IQM\text{-}Garnet}$

Appendix H: Quantum Parameter Efficiency and Quantum Memory Advantage

This section explain the parameter efficiency and memory advantage for the QIML. According to the parameter numbers in this work, as shown in table IV, we used 120 parameters on the KS system, 180 on the Kolmogorov flows on the emulator, and 240 or 300 for the TCF system on the hardware and emulator. As is evident, our method uses a remarkably small number of parameters to learn the necessary statistical information. We have already shown the orders-of-magnitude difference in parameter counts compared to classical models in table III. Both the parameter efficiency discussed here and the memory advantage that follows originate from the same foundational quantum advantage [65]: the ability of a quantum circuit to logarithmically compress classical data. This is the fundamental source of the quantum advantage established in our work, a topic we have discussed in detail in Sec. VI. The critical challenge in harnessing this advantage is circumventing the limitations imposed by Holevo's bound. This bound arises because retrieving the complete classical information from the quantum state would necessitate an exponential number of measurements, rendering the approach impractical. This obstacle is overcome because the task of guiding a dynamical model does not necessitate access to the complete classical dataset. Instead, the framework's objective is to extract a statistical summary, the distribution of velocity information, which represents the system's invariant measure. For a chaotic system, such a measure inherently contains far less information than the full dataset from which it is derived. The ability to function with only this compressed distributional information allows the method to bypass the need for an exponential number of measurements. This principle is the foundation for the quantum memory advantage, which is now detailed for the three systems investigated in this paper.

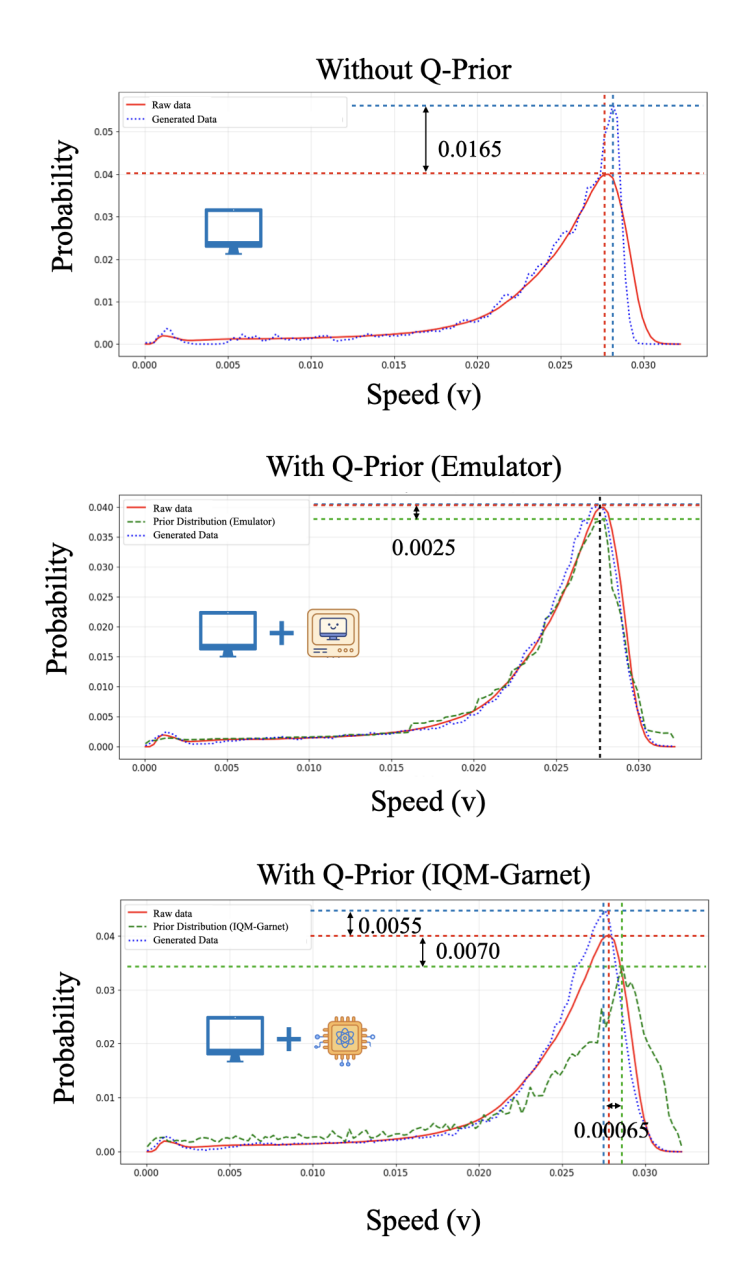


FIG. 15. Diagram of the velocity distribution of the turbulent channel flow predicted under the same three learning regimes (no Q-Prior, emulator-based Q-Prior, and IQM hardware-based Q-Prior), compared to the target distribution. Without quantum guidance, the model fails to capture the dominant statistical mode—both the modal peak and its amplitude are significantly misaligned. With Q-Prior, the predicted distribution nearly perfectly matches the raw data.

## 1. Kuramoto-Sivashinsky Equation

The raw KS data comprise 1200 trajectories, each recorded for 2000 time steps on a 512-point spatial grid, totalling  $\sim 12.3\,\mathrm{GB}$ . For training we down-sample to  $N_{\mathrm{traj}} = 1200$  trajectories, each with 256 temporal frames and 128 spatial points, leading to a working tensor of shape (256, 128) per trajectory. With double precision (8 bytes per value) a single trajectory occupies

$$256 \times 128 \times 8 = 2.62 \times 10^5 \text{ bytes} \simeq 0.25 \text{ MB}.$$
 (H1)

Thus, the full down-sampled dataset requires  $0.25 \,\mathrm{MB} \times 1200 \approx 300 \,\mathrm{MB}$ . Each trajectory is paired with an individual quantum generator containing n=10 qubits, L=4 circuit layers and 120 rotation parameters, for a raw weight file of  $120 \times 8 = 960$  bytes; including metadata the stored checkpoint is  $\approx 1.0 \,\mathrm{kB}$ . Archiving one checkpoint per trajectory,

therefore, costs  $1200 \times 1.0\,\mathrm{kB} \approx 1.2\,\mathrm{MB}$ . Consequently, the learned Q-Priors reduce storage from  $\sim 300\,\mathrm{MB}$  to  $\sim 1.2\,\mathrm{MB}$ , a compression factor of around 250:1 while still capturing the essential statistics used by the classical machine learning model.

## 2. 2D Kolmogorov Flows

The total dataset comprises 40 trajectories, each containing 320 temporal snapshots on a  $256 \times 256$  grid. For a single velocity component, one snapshot occupies

$$256^2 \times 8 = 524,288 \text{ bytes} \simeq 0.50 \text{ MB}.$$
 (H2)

so that one complete trajectory requires  $0.50~\mathrm{MB} \times 320 \approx 160~\mathrm{MB}$  and the full set of 40 trajectories stores  $\sim 6.4~\mathrm{GB}$ . The corresponding quantum generator employs n=10 qubits, L=6 layers and 180 trainable rotation angles. Saved in double precision, one checkpoint is  $180\times8=1,440~\mathrm{bytes}\simeq1.4~\mathrm{kB}$ . Archiving a separate checkpoint for every snapshot therefore costs

$$1.4 \text{ kB} \times 320 = 448 \text{ kB} \simeq 0.44 \text{ MB}.$$
 (H3)

yielding a compression factor of

$$\frac{160 \text{ MB}}{0.44 \text{ MB}} \approx 3.6 \times 10^2.$$
 (H4)

while faithfully reproducing the empirical invariant measure.

#### 3. Turbulent Channel Flow

For the TCF benchmark, each snapshot is stored as a  $192 \times 192$  array of double-precision values (8 bytes per entry). A single velocity component therefore, occupies

$$192^2 \times 8 = 294,912 \text{ bytes} \simeq 0.29 \text{ MB}.$$
 (H5)

so that the full sequence of 595 snapshots amounts to

$$0.29 \text{ MB} \times 595 \approx 170 \text{ MB}. \tag{H6}$$

Retaining all three velocity components raises the per-trajectory footprint to roughly 500 MB.

The quantum generators used to reproduce the same invariant statistics each employ n=15 qubits, L=6 layers, and 240 rotation angles. Each saved quantum generator checkpoint, with minimal metadata, is about 4.3 kB. Given that 595 such quantum generator models are retained (one for each snapshot), the total storage for the entire set of quantum generator checkpoints amounts to  $595 \times 4.3 \,\mathrm{kB} \approx 2.5 \,\mathrm{MB}$ . Relative to the raw three-component trajectory ( $\sim 500 \,\mathrm{MB}$ ), this represents a compression factor of approximately 200, which is over two orders of magnitude, while still capturing the statistics required by the classical Koopman machine learning model.

## Appendix I: Performance and Statistical Metrics

This section provides the mathematical definitions for the primary metrics used in this paper to evaluate model performance and analyse the system's statistical properties.

#### 1. Temporal Autocorrelation

The temporal autocorrelation is used to measure the memory of the dynamical system, quantifying the correlation of a time series with a delayed version of itself. For a discrete time series  $u_i$  (the value at a specific spatial point at time step i), with mean  $\bar{u}$  and total length N, the normalized temporal autocorrelation C(k) at a time lag of k steps is defined as:

$$C(k) = \frac{\sum_{i=1}^{N-k} (u_i - \bar{u})(u_{i+k} - \bar{u})}{\sum_{i=1}^{N} (u_i - \bar{u})^2}$$
(I1)

## 2. Error Metrics

To quantify the difference between the ground truth data and the model predictions, the following error metrics are used.

The absolute error provides a direct, point-wise measure of the deviation between a predicted field  $\hat{u}(\mathbf{x})$  and the ground truth field  $u(\mathbf{x})$ :

$$E_{\text{abs}}(\mathbf{x}) = |u(\mathbf{x}) - \hat{u}(\mathbf{x})| \tag{I2}$$

To specifically quantify how well the model reproduces the temporal correlation structure, we define the normalized relative auto-correlation error  $E_r$ . This measures the relative L2 error between the true autocorrelation function  $C_{\text{true}}(k)$  and the predicted one  $C_{\text{pred}}(k)$ :

$$E_r = \frac{\|C_{\text{true}}(k) - C_{\text{pred}}(k)\|_2}{\|C_{\text{true}}(k)\|_2}$$
(I3)

- L. Biferale, G. Boffetta, A. Celani, B. Devenish, A. Lanotte, and F. Toschi, Multifractal statistics of lagrangian velocity and acceleration in turbulence, Physical Review Letters 93, 064502 (2004).
- [2] V. A. Galaktionov and J. L. Vázquez, A stability technique for evolution partial differential equations: a dynamical systems approach, Vol. 56 (Springer Science & Business Media, 2012).
- [3] Z. Long, Y. Lu, X. Ma, and B. Dong, Pde-net: Learning pdes from data, in *International conference on machine* learning (PMLR, 2018) pp. 3208–3216.
- [4] H. Bergström, H. Alfredsson, J. Arnqvist, I. Carlén, E. Dellwik, J. Fransson, H. Ganander, M. Mohr, A. Segalini, and S. Söderberg, Wind power in forests: wind and effects on loads (2013).
- [5] P. V. Coveney, Sharkovskii's theorem and the limits of digital computers for the simulation of chaotic dynamical systems, Journal of Computational Science 83, 102449 (2024).
- [6] M. Klöwer, P. V. Coveney, E. A. Paxton, and T. N. Palmer, Periodic orbits in chaotic systems simulated at low precision, Scientific Reports 13, 11410 (2023).
- [7] B. M. Boghosian, P. V. Coveney, and H. Wang, A new pathology in the simulation of chaotic dynamical systems on digital computers, Advanced Theory and Simulations 2, 1900125 (2019).
- [8] P. V. Coveney and S. Wan, Molecular Dynamics: Probability and Uncertainty (Oxford University Press, 2025).
- [9] D. Kalla, N. Smith, F. Samaah, and S. Kuraku, Study and analysis of chat gpt and its impact on different fields of study, International Journal of Innovative Science and Research Technology 8 (2023).
- [10] E. Kasneci, K. Seßler, S. Küchemann, M. Bannert, D. Dementieva, F. Fischer, U. Gasser, G. Groh, S. Günnemann, E. Hüllermeier, et al., ChatGPT for good? on opportunities and challenges of large language models for education, Learning and Individual Differences 103, 102274 (2023).
- [11] Y. Chang, X. Wang, J. Wang, Y. Wu, L. Yang, K. Zhu, H. Chen, X. Yi, C. Wang, Y. Wang, et al., A survey on evaluation of large language models, ACM Transactions on Intelligent Systems and Technology 15, 1 (2024).
- [12] A. J. Thirunavukarasu, D. S. J. Ting, K. Elangovan, L. Gutierrez, T. F. Tan, and D. S. W. Ting, Large language models in medicine, Nature Medicine 29, 1930 (2023).
- [13] A. Voulodimos, N. Doulamis, A. Doulamis, and E. Protopapadakis, Deep learning for computer vision: A brief review, Computational Intelligence and Neuroscience 2018, 7068349 (2018).
- [14] J. Zhang, J. Huang, S. Jin, and S. Lu, Vision-language models for vision tasks: A survey, IEEE Transactions on Pattern Analysis and Machine Intelligence 46, 5625 (2024).
- [15] K. Zhou, J. Yang, C. C. Loy, and Z. Liu, Learning to prompt for vision-language models, International Journal of Computer Vision 130, 2337 (2022).
- [16] P. Zhang, X. Li, X. Hu, J. Yang, L. Zhang, L. Wang, Y. Choi, and J. Gao, Vinvl: Revisiting visual representations in vision-language models, in *Proceedings of the IEEE/CVF conference on computer vision and pattern*

- recognition (2021) pp. 5579-5588.
- [17] I. Price, A. Sanchez-Gonzalez, F. Alet, T. R. Andersson, A. El-Kadi, D. Masters, T. Ewalds, J. Stott, S. Mohamed, P. Battaglia, et al., Probabilistic weather forecasting with machine learning, Nature 637, 84 (2025).
- [18] K. Bi, L. Xie, H. Zhang, X. Chen, X. Gu, and Q. Tian, Accurate medium-range global weather forecasting with 3d neural networks, Nature 619, 533 (2023).
- [19] R. Lam, A. Sanchez-Gonzalez, M. Willson, P. Wirnsberger, M. Fortunato, F. Alet, S. Ravuri, T. Ewalds, Z. Eaton-Rosen, W. Hu, et al., Learning skillful medium-range global weather forecasting, Science 382, 1416 (2023).
- [20] M. Cavaiola, F. Cassola, D. Sacchetti, F. Ferrari, and A. Mazzino, Hybrid ai-enhanced lightning flash prediction in the medium-range forecast horizon, Nature Communications 15, 1188 (2024).
- [21] S. L. Brunton, B. R. Noack, and P. Koumoutsakos, Machine learning for fluid mechanics, Annual Review of Fluid Mechanics 52, 477 (2020).
- [22] H. J. Bae and P. Koumoutsakos, Scientific multi-agent reinforcement learning for wall-models of turbulent flows, Nature Communications 13, 1443 (2022).
- [23] X. Yang, S. Zafar, J.-X. Wang, and H. Xiao, Predictive large-eddy-simulation wall modeling via physics-informed neural networks, Physical Review Fluids 4, 034602 (2019).
- [24] X. Xue, S. Wang, H.-D. Yao, L. Davidson, and P. V. Coveney, Physics informed data-driven near-wall modelling for lattice Boltzmann simulation of high reynolds number turbulent flows, Communications Physics 7, 338 (2024).
- [25] R. Maulik, O. San, J. D. Jacob, and C. Crick, Sub-grid scale model classification and blending through deep learning, Journal of Fluid Mechanics 870, 784 (2019).
- [26] A. Pal, Deep learning emulation of subgrid-scale processes in turbulent shear flows, Geophysical Research Letters 47, e2020GL087005 (2020).
- [27] K. Fukami, Y. Nabae, K. Kawai, and K. Fukagata, Synthetic turbulent inflow generator using machine learning, Physical Review Fluids 4, 064603 (2019).
- [28] M. Z. Yousif, L. Yu, and H. Lim, Physics-guided deep learning for generating turbulent inflow conditions, Journal of Fluid Mechanics 936, A21 (2022).
- [29] M. Raissi, P. Perdikaris, and G. E. Karniadakis, Physics-informed neural networks: A deep learning framework for solving forward and inverse problems involving nonlinear partial differential equations, Journal of Computational Physics 378, 686 (2019).
- [30] I. Goodfellow, J. Pouget-Abadie, M. Mirza, B. Xu, D. Warde-Farley, S. Ozair, A. Courville, and Y. Bengio, Generative adversarial networks, Communications of the ACM 63, 139 (2020).
- [31] L. Lu, P. Jin, G. Pang, Z. Zhang, and G. E. Karniadakis, Learning nonlinear operators via deeponet based on the universal approximation theorem of operators, Nature Machine Intelligence 3, 218 (2021).
- [32] Z. Li, N. Kovachki, K. Azizzadenesheli, B. Liu, K. Bhattacharya, A. Stuart, and A. Anandkumar, Fourier neural operator for parametric partial differential equations, arXiv preprint arXiv:2010.08895 (2020).

- [33] V. Vanchurin, Toward a theory of machine learning, Machine Learning: Science and Technology 2, 035012 (2021).
- [34] G. Carleo, I. Cirac, K. Cranmer, L. Daudet, M. Schuld, N. Tishby, L. Vogt-Maranto, and L. Zdeborová, Machine learning and the physical sciences, Reviews of Modern Physics 91, 045002 (2019).
- [35] Y. Schiff, Z. Y. Wan, J. B. Parker, S. Hoyer, V. Kuleshov, F. Sha, and L. Zepeda-Núñez, Dyslim: Dynamics Stable Learning by Invariant Measure for Chaotic Systems, arXiv preprint arXiv:2402.04467 (2024).
- [36] M. Cerezo, G. Verdon, H.-Y. Huang, L. Cincio, and P. J. Coles, Challenges and opportunities in quantum machine learning, Nature Computational Science 2, 567 (2022).
- [37] X. Gao, E. R. Anschuetz, S.-T. Wang, J. I. Cirac, and M. D. Lukin, Enhancing generative models via quantum correlations, Physical Review X 12, 021037 (2022).
- [38] J. Tilly, H. Chen, S. Cao, D. Picozzi, K. Setia, Y. Li, E. Grant, L. Wossnig, I. Rungger, G. H. Booth, et al., The variational quantum eigensolver: a review of methods and best practices, Physics Reports 986, 1 (2022).
- [39] A. Kandala, A. Mezzacapo, K. Temme, M. Takita, M. Brink, J. M. Chow, and J. M. Gambetta, Hardwareefficient variational quantum eigensolver for small molecules and quantum magnets, Nature 549, 242 (2017).
- [40] P. J. O'Malley, R. Babbush, I. D. Kivlichan, J. Romero, J. R. McClean, R. Barends, J. Kelly, P. Roushan, A. Tranter, N. Ding, et al., Scalable quantum simulation of molecular energies, Physical Review X 6, 031007 (2016).
- [41] J. Stokes, J. Izaac, N. Killoran, and G. Carleo, Quantum natural gradient, Quantum 4, 269 (2020).
- [42] E. Farhi, J. Goldstone, and S. Gutmann, A quantum approximate optimization algorithm, arXiv preprint arXiv:1411.4028 (2014).
- [43] S. Sanyal and K. Roy, Neuro-Ising: Accelerating largescale traveling salesman problems via graph neural network guided localized Ising solvers, IEEE Transactions on Computer-Aided Design of Integrated Circuits and Systems 41, 5408 (2022).
- [44] M. G. Vakili, C. Gorgulla, A. Nigam, D. Bezrukov, D. Varoli, A. Aliper, D. Polykovsky, K. M. P. Das, J. Snider, A. Lyakisheva, et al., Quantum computingenhanced algorithm unveils novel inhibitors for kras, arXiv preprint arXiv:2402.08210 (2024).
- [45] J. Romero and A. Aspuru-Guzik, Variational quantum generators: Generative adversarial quantum machine learning for continuous distributions, Advanced Quantum Technologies 4, 2000003 (2021).
- [46] P.-L. Dallaire-Demers and N. Killoran, Quantum generative adversarial networks, Physical Review Applied 8, 024012 (2018).
- [47] M. Benedetti, E. Lloyd, S. Sack, and M. Fiorentini, Parameterized quantum circuits as machine learning models, Quantum Science and Technology 4, 043001 (2019).
- [48] J. Preskill, Quantum computing in the NISQ era and beyond, Quantum 2, 79 (2018).
- [49] T. Kubař, M. Elstner, and Q. Cui, Hybrid quantum mechanical/molecular mechanical methods for studying energy transduction in biomolecular machines, Annual Review of Biophysics 52, 525 (2023).

- [50] L. Böselt, M. Thürlemann, and S. Riniker, Machine learning in QM/MM molecular dynamics simulations of condensed-phase systems, Journal of Chemical Theory and Computation 17, 2641 (2021).
- [51] R. P. Magalhães, H. S. Fernandes, and S. F. Sousa, Modelling enzymatic mechanisms with QM/MM approaches: current status and future challenges, Israel Journal of Chemistry 60, 655 (2020).
- [52] T. M. Bickley, A. Mingare, T. Weaving, M. W. de la Bastida, S. Wan, M. Nibbi, P. Seitz, A. Ralli, P. J. Love, M. Chung, et al., Extending quantum computing through subspace, embedding and classical molecular dynamics techniques, arXiv preprint arXiv:2505.16796 (2025).
- [53] M. Ghazi Vakili, C. Gorgulla, J. Snider, A. Nigam, D. Bezrukov, D. Varoli, A. Aliper, D. Polykovsky, K. M. Padmanabha Das, H. Cox Iii, et al., Quantumcomputing-enhanced algorithm unveils potential kras inhibitors, Nature Biotechnology, 1 (2025).
- [54] J.-G. Liu and L. Wang, Differentiable learning of quantum circuit born machines, Physical Review A 98, 062324 (2018).
- [55] M. Benedetti, D. Garcia-Pintos, O. Perdomo, V. Leyton-Ortega, Y. Nam, and A. Perdomo-Ortiz, A generative modeling approach for benchmarking and training shallow quantum circuits, npj Quantum Information 5, 45 (2019).
- [56] A. Gretton, K. M. Borgwardt, M. J. Rasch, B. Schölkopf, and A. Smola, A kernel two-sample test, The Journal of Machine Learning Research 13, 723 (2012).
- [57] M. Budišić, R. Mohr, and I. Mezić, Applied koopmanism, Chaos: An Interdisciplinary Journal of Nonlinear Science 22 (2012).
- [58] I. Mezić, Koopman operator, geometry, and learning of dynamical systems, Not. Am. Math. Soc 68, 1087 (2021).
- [59] S. L. Brunton, M. Budišić, E. Kaiser, and J. N. Kutz, Modern Koopman theory for dynamical systems, arXiv preprint arXiv:2102.12086 (2021).
- [60] K. E. Petersen and K. Petersen, Ergodic theory (Cambridge university press, 1989).
- [61] X. Cheng, Y. He, Y. Yang, X. Xue, S. Cheng, D. Giles, X. Tang, and Y. Hu, Learning chaos in a linear way, arXiv preprint arXiv:2503.14702 (2025).
- [62] G. D. Birkhoff, Proof of the ergodic theorem, Proceedings of the National Academy of Sciences 17, 656 (1931).
- [63] J. von Neumann, Proof of the quasi-ergodic hypothesis, Proceedings of the National Academy of Sciences 18, 70 (1932).
- [64] R. Pascanu, T. Mikolov, and Y. Bengio, On the difficulty of training recurrent neural networks, in *International* conference on machine learning (2013) pp. 1310–1318.
- [65] H.-Y. Huang, S. Choi, J. R. McClean, and J. Preskill, The vast world of quantum advantage, arXiv preprint arXiv:2508.05720 (2025).
- [66] M. Wang, J. Jiang, and P. V. Coveney, A parameterefficient quantum anomaly detection method on a superconducting quantum processor, arXiv preprint arXiv:2412.16867 (2024).
- [67] H.-Y. Huang, M. Broughton, J. Cotler, S. Chen, J. Li, M. Mohseni, H. Neven, R. Babbush, R. Kueng, J. Preskill, et al., Quantum advantage in learning from experiments, Science 376, 1182 (2022).

- [68] F. Marxer, A. Vepsäläinen, S. W. Jolin, J. Tuorila, A. Landra, C. Ockeloen-Korppi, W. Liu, O. Ahonen, A. Auer, L. Belzane, et al., Long-distance transmon coupler with cz-gate fidelity above 99.8%, PRX Quantum 4, 010314 (2023).
- [69] L. Abdurakhimov, J. Adam, H. Ahmad, O. Ahonen, M. Algaba, G. Alonso, V. Bergholm, R. Beriwal, M. Beuerle, C. Bockstiegel, et al., Technology and performance benchmarks of iqm's 20-qubit quantum computer, arXiv preprint arXiv:2408.12433 (2024).
- [70] P. D. Nation, H. Kang, N. Sundaresan, and J. M. Gambetta, Scalable mitigation of measurement errors on quantum computers, PRX Quantum 2, 040326 (2021).
- [71] C. Zhu, R. H. Byrd, P. Lu, and J. Nocedal, Algorithm 778: L-bfgs-b: Fortran subroutines for large-scale bound-constrained optimization, ACM Transactions on Mathematical Software 23, 550 (1997).
- [72] Z. Zhang, Improved Adam optimizer for deep neural networks, in 2018 IEEE/ACM 26th international symposium on quality of service (IWQoS) (Ieee, 2018) pp. 1–2.
- [73] R. G. Regis, Stochastic radial basis function algorithms for large-scale optimization involving expensive blackbox objective and constraint functions, Computers & Operations Research 38, 837 (2011).
- [74] S. Succi, The Lattice Boltzmann Equation for Fluid Dynamics and Beyond (Oxford University Press, 2001).
- [75] R. D. Moser, J. Kim, and N. N. Mansour, Direct numerical simulation of turbulent channel flow up to  $re_{\tau} = 590$ , Physics of Fluids **11**, 943 (1999).
- [76] S. Chen and G. D. Doolen, Lattice Boltzmann method for fluid flows, Annual Review of Fluid Mechanics 30, 329 (1998).
- [77] X. Xue, H.-D. Yao, and L. Davidson, Synthetic turbulence generator for lattice Boltzmann method at the interface between rans and LES, Physics of Fluids 34, 055118 (2022).
- [78] Z. Li, M. Liu-Schiaffini, N. Kovachki, B. Liu, K. Aziz-zadenesheli, K. Bhattacharya, A. Stuart, and A. Anand-kumar, Learning dissipative dynamics in chaotic systems, arXiv preprint arXiv:2106.06898 (2021).
- [79] A. R. Barron, Universal approximation bounds for superpositions of a sigmoidal function, IEEE Transactions on Information Theory 39, 930 (2002).
- [80] I. Goodfellow, Y. Bengio, and A. Courville, Deep Learning (MIT Press, 2016) Chap. 6.
- [81] S. Jerbi, C. Gyurik, S. C. Marshall, R. Molteni, and V. Dunjko, Shadows of quantum machine learning, Nature Communications 15, 5676 (2024).
- [82] P. W. Shor, Polynomial-time algorithms for prime factorization and discrete logarithms on a quantum computer, SIAM review 41, 303 (1999).
- [83] A. W. Harrow, A. Hassidim, and S. Lloyd, Quantum algorithm for linear systems of equations, Physical Review Letters 103, 150502 (2009).
- [84] D. Gilboa, H. Michaeli, D. Soudry, and J. McClean, Exponential quantum communication advantage in distributed inference and learning, Advances in Neural Information Processing Systems 37, 30425 (2024).
- [85] A. S. Holevo, Bounds for the quantity of information transmitted by a quantum communication channel, Problemy Peredachi Informatsii 9, 3 (1973).
- [86] I. P. Cornfeld, S. V. Fomin, and Y. G. Sinai, Ergodic theory, Vol. 245 (Springer Science & Business Media,

- 2012).
- [87] M. C. Caro, H.-Y. Huang, N. Ezzell, J. Gibbs, A. T. Sornborger, L. Cincio, P. J. Coles, and Z. Holmes, Out-of-distribution generalization for learning quantum dynamics, Nature Communications 14, 3751 (2023).
- [88] C. S. Calude and G. Longo, The deluge of spurious correlations in big data, Foundations of Science 22, 595 (2017).
- [89] J. Romero, J. P. Olson, and A. Aspuru-Guzik, Quantum autoencoders for efficient compression of quantum data, Quantum Science and Technology 2, 045001 (2017).
- [90] L. Lamata, U. Alvarez-Rodriguez, J. D. Martín-Guerrero, M. Sanz, and E. Solano, Quantum autoencoders via quantum adders with genetic algorithms, Quantum Science and Technology 4, 014007 (2018).
- [91] Y. Ding, L. Lamata, M. Sanz, X. Chen, and E. Solano, Experimental implementation of a quantum autoencoder via quantum adders, Advanced Quantum Technologies 2, 1800065 (2019).
- [92] M. Kieferová and N. Wiebe, Tomography and generative training with quantum boltzmann machines, Physical Review A 96, 062327 (2017).
- [93] S. Jain, J. Ziauddin, P. Leonchyk, S. Yenkanchi, and J. Geraci, Quantum and classical machine learning for the classification of non-small-cell lung cancer patients, SN Applied Sciences 2, 1 (2020).
- [94] P.-L. Dallaire-Demers and N. Killoran, Quantum generative adversarial networks, Physical Review A 98, 012324 (2018).
- [95] J. Zeng, Y. Wu, J.-G. Liu, L. Wang, and J. Hu, Learning and inference on generative adversarial quantum circuits, Physical Review A 99, 052306 (2019).
- [96] P. Rebentrost, M. Mohseni, and S. Lloyd, Quantum support vector machine for big data classification, Physical Review Letters 113, 130503 (2014).
- [97] R. Mengoni and A. Di Pierro, Kernel methods in quantum machine learning, Quantum Machine Intelligence 1, 65 (2019).
- [98] H.-Y. Huang, M. Broughton, M. Mohseni, R. Babbush, S. Boixo, H. Neven, and J. R. McClean, Power of data in quantum machine learning, Nature Communications 12, 1 (2021).
- [99] J. Carrasquilla, G. Torlai, R. G. Melko, and L. Aolita, Reconstructing quantum states with generative models, Nature Machine Intelligence 1, 155 (2019).
- [100] X. Gao, Z.-Y. Zhang, and L.-M. Duan, A quantum machine learning algorithm based on generative models, Science Advances 4, eaat9004 (2018).
- [101] Y. Kuramoto, Chemical oscillations, waves, and turbulence (Courier Corporation, 2003).
- [102] G. I. Sivashinsky, On flame propagation under conditions of stoichiometry, SIAM Journal on Applied Mathematics 39, 67 (1980).
- [103] D. Kochkov, J. A. Smith, A. Alieva, Q. Wang, M. P. Brenner, and S. Hoyer, Machine learning-accelerated computational fluid dynamics, Proceedings of the National Academy of Sciences 118, 10.1073/pnas.2101784118 (2021).
- [104] G. J. Chandler and R. R. Kerswell, Invariant recurrent solutions embedded in a turbulent two-dimensional kolmogorov flow, Journal of Fluid Mechanics 722, 554 (2013).
- [105] J. Smagorinsky, General circulation experiments with the primitive equations: I. the basic experiment,

- Monthly Weather Review 91, 99 (1963).
- [106] S. Hou, J. Sterling, S. Chen, and G. Doolen, A lattice Boltzmann subgrid model for high Reynolds number flows, Pattern Formation and Lattice Gas Automata, 151 (1995).
- [107] Y. Koda and F.-S. Lien, The lattice Boltzmann method implemented on the GPU to simulate the turbulent flow over a square cylinder confined in a channel, Flow, Turbulence and Combustion 94, 495 (2015).
- [108] J. Latt, B. Chopard, O. Malaspinas, M. Deville, and A. Michler, Straight velocity boundaries in the lattice Boltzmann method, Physical Review E 77, 056703 (2008).
- [109] D. d'Humieres, Multiple-relaxation-time lattice Boltzmann models in three dimensions, Philosophical Transactions of the Royal Society of London. Series A: Mathematical, Physical and Engineering Sciences 360, 437 (2002).